AB INITIO QUANTUM MOLECULAR DYNAMICS

MICHAL BEN-NUN and TODD. J. MARTÍNEZ

Department of Chemistry and the Beckman Institute, University of Illinois, Urbana, Illinois, U.S.A.

CONTENTS

I. INTRODUCTION

The introduction of the Born–Oppenheimer approximation (BOA) set the stage for the development of electronic structure theory and molecular dynamics as separate disciplines. Certainly this separation has been fruitful and has in large measure fostered the rapid development of the fields. However, it is also clear that a comprehensive approach to chemistry must remain cognizant of the interplay between electronic structure and nuclear dynamics. Inferring dynamical behavior

Advances in Chemical Physics, Volume 121, Edited by I. Prigogine and Stuart A. Rice.
ISBN 0-471-20504-4

from potential energy surfaces (PESs) can be deceptive, especially when energy flow is restricted on the relevant timescales. The subpicosecond lifetimes often observed for excited electronic state dynamics imply that this caution will be especially valid in photochemistry. On the other hand, fitting of multidimensional PESs to empirical functional forms involves a tradeoff between accuracy and human effort. Erasing the boundary between electronic structure and molecular dynamics is the goal of *ab initio* molecular dynamics (AIMD) methods, which are just entering mainstream chemical physics because of recent methodological and computational advances. Simultaneous solution of the electronic Schrödinger equation and Newton's equations reemphasizes the close relationship between the electrons that govern the form of the PES and the nuclear dynamics that occurs on this PES. From a practical standpoint, arbitrary bond rearrangements can be described without difficult and often impossible fitting procedures. The first AIMD calculation [1] was performed in the 1970s, with the quantum chemical part of the calculation treated largely as a complicated and computationally expensive force routine. The introduction of the Car-Parrinello (CP) method [2] fueled the rapid increase in popularity of AIMD methods over the last 15 years [3–7], although we hasten to add that not all AIMD methods use the extended Lagrangian scheme which is the hallmark of the CP method [8–13]. Interestingly, the core of the CP method is a blurring of the line separating electronic structure and molecular dynamics. The coefficients that comprise the unknowns in the quantum chemical problem are endowed with a fictitious dynamics designed to mimic complete solution of the electronic structure at every time step. We believe that this trend will continue, and there is hope that it will lead to a better understanding of the interplay between electronic and nuclear motion.

Most of the AIMD simulations described in the literature have assumed that Newtonian dynamics was sufficient for the nuclei. While this is often justified, there are important cases where the quantum mechanical nature of the nuclei is crucial for even a qualitative understanding. For example, tunneling is intrinsically quantum mechanical and can be important in chemistry involving proton transfer. A second area where nuclei must be described quantum mechanically is when the BOA breaks down, as is always the case when multiple coupled electronic states participate in chemistry. In particular, photochemical processes are often dominated by conical intersections [14,15], where two electronic states are exactly degenerate and the BOA fails. In this chapter, we discuss our recent development of the *ab initio* multiple spawning (AIMS) method which solves the elecronic and nuclear Schrödinger equations simultaneously; this makes AIMD approaches applicable for problems where quantum mechanical effects of both electrons and nuclei are important. We present an overview of what has been achieved, and make a special effort to point out areas where further improvements can be made. Theoretical aspects of the AIMS method are

discussed, including both the electronic and nuclear parts of the problem. Several applications to fundamental problems in the chemistry of excited electronic states are presented, and we conclude with our thoughts on future interesting directions.

II. THEORY

The development of an *ab initio* quantum molecular dynamics method is guided by the need to overcome two main obstacles. First, one needs to develop an efficient, yet accurate, method for solving the electronic Schrödinger equation for both ground and excited electronic states. Second, the quantum mechanical character of the nuclear dynamics must be addressed. (This is necessary for the description of photochemical and tunneling processes.) This section provides a detailed discussion of the approaches we have taken to solve these two problems.

A. Electronic Structure for Multiple Electronic States

A first-principles treatment of photochemistry requires repeated solution of the electronic Schrödinger equation for multiple electronic states, including the nonadiabatic coupling matrix elements that induce transitions between electronic states. These requirements make computational efficiency paramount, even more so than for traditional time-independent quantum chemistry. At the same time, accuracy must be maintained because there is no point in developing a first-principles approach if the underlying PESs are *not* (at least) qualitatively accurate. The conflicting requirements of accuracy and efficiency are already present in time-independent quantum chemistry, but they are made more severe in the time-dependent case because of both the large number of PES evaluations and the requirement of global accuracy in the PESs.

Single-reference methods, such as single-excitation configuration interaction (CIS) [16,17], are computationally attractive and in certain circumstances are capable of describing both ground and excited electronic states. These methods often provide reasonable vertical excitation energies for the excited states that dominate electronic absorption spectra. However, the accuracy, and hence utility, of single-reference methods in general, and single-reference/single-excitation methods in particular, diminishes rapidly as the excited-state trajectory/wavefunction leaves the Franck–Condon region. This is due to two problems. First, while electronic states with doubly excited character are usually optically forbidden (and hence less important in the electronic absorption spectrum), they can play a significant role in photochemistry and cannot be modeled accurately with CIS. Second, avoided crossings and conical intersections are often ubiquitous in the manifold of excited states. Even if the wavefunctions for each of the interacting states are reasonably described by a single configuration outside the crossing/intersection region, a multireference description becomes necessary in these regions because

the character of the wavefunctions changes rapidly. For example, CIS fails to correctly predict the global minimum on the lowest-valence adiabatic excited-state surface of ethylene [18]. Despite their computational advantages, most single-reference methods are not appropriate for our needs because of their inability to predict the correct shape of the excited potential energy surface(s). It remains to be seen whether these criticisms apply to time-dependent formulations of density functional theory (TDDFT) [19–21], which are superficially similar to single-reference/single-excitation methods.

A further problem in *ab initio* photochemistry is the need to avoid variational bias to the ground electronic state; that is, the quality of the ground- and excited-state wavefunctions should be similar. A widely used procedure that alleviates this problem is state-averaging [22–25]. Here the orbitals are determined to minimize a weighted average of the ground-state and one or more excited-state energies. The resulting orbitals are often called a "best-compromise" set because they are *not* optimal for *any* single target electronic state. Once the orbitals have been determined, state-dependent orbital relaxation must be incorporated, typically via the inclusion of single excitations in a configuration interaction wavefunction. In this approach, single excitations are taken from the same set of reference configurations that was used to determine the orbitals in the state-averaged multiconfiguration SCF (MCSCF). Variants of this technique, such as the first-order CI method of Schaefer [26] and the POL-CI method of Goddard [27], have been successfully used in past treatments of excited states.

A simpler computational procedure with similar aims is occupation averaging. Here, the orbitals that are of variable occupancy (comprising the "active space") in the ground and excited electronic states are equally populated with electrons. (For example, in the case of $\pi \rightarrow \pi^*$ excitation of ethylene or cyclobutene, the π and π^* orbitals would each be singly occupied.) There are several ways to accomplish this averaging, differing in the treatment of electronic spin coupling. The active space orbitals may be determined by an SCF procedure where they are high-spin coupled in a single determinant. This approach is related to "half-electron" semiempirical theories [28], and similarly motivated approaches have recently been investigated in coupled cluster methods [29]. For ethylene with a two-orbital active space, this corresponds to using the SCF orbitals from a triplet single-determinant wavefunction. This procedure has been tested for ethylene, where the lowest triplet Hartree–Fock wavefunction is less prone than the ground-state singlet wavefunction to overemphasize Rydberg character in the orbitals. It has therefore been argued that the triplet coupled orbitals provide a better starting point for CI expansions [30]. A second approach for the specific case of ethylene determines the orbitals using the framework of a generalized valence bond (GVB) wavefunction [31] where the covalent and ionic states are constrained to have equal weights. For

example, the GVB wavefunction for ethylene is

$$\psi_{\mathrm{GVB}} = c_{\mathrm{cov}}\hat{A}[\psi_{\mathrm{core}}(\chi_{Cp,r}\chi_{Cp,l} + \chi_{Cp,l}\chi_{Cp,r})(\alpha\beta - \beta\alpha)] + c_{\mathrm{ion}}\hat{A}[\psi_{\mathrm{core}}(\chi_{Cp,r}\chi_{Cp,r} + \chi_{Cp,l}\chi_{Cp,l})(\alpha\beta - \beta\alpha)] \tag{2.1}$$

where $\hat{A}$ is the antisymmetrizing operator, ψ_{core} represents all the σ framework electrons, and $\chi_{Cp,r}$ and $\chi_{Cp,l}$ denote the nonorthogonal GVB orbitals on the right and left carbon atoms (respectively), which are dominated by contributions from the carbon $2p$ atomic orbitals. The GVB wavefunction, Eq. (2.1), can be written in an equivalent form using the orthogonal molecular orbitals:

$$\psi_{\mathrm{GVB}} = c_b\hat{A}[\psi_{\mathrm{core}}\phi_\pi\phi_\pi(\alpha\beta - \beta\alpha)] + c_a\hat{A}[\psi_{\mathrm{core}}\phi_{\pi^*}\phi_{\pi^*}(\alpha\beta - \beta\alpha)] \tag{2.2}$$

In the usual GVB procedure, both the orbitals and the coefficients $c_{\mathrm{cov}}, c_{\mathrm{ion}}$ or, equivalently, c_b, c_a would be optimized. The occupation-averaged orbitals appropriate for the GVB wavefunction are defined to minimize the average energy of the individual terms in Eq. (2.2):

$$E_{\mathrm{average}} = 1/2[E(\psi_{\mathrm{core}}\phi_\pi\phi_\pi) + E(\psi_{\mathrm{core}}\phi_{\pi^*}\phi_{\pi^*})] \tag{2.3}$$

Theoretically, this is somewhat more appealing than the use of triplet orbitals, because the orbitals in this procedure are derived from a wavefunction averaged over states with the desired singlet spin coupling. In our studies on ethylene, we have found little difference between the two approaches. For example, the global features of the PESs are qualitatively unchanged for these two choices of starting orbitals, and even the vertical excitation energies are within 0.1 of each other. This is apparently due to the subsequent CI expansion, which is sufficiently flexible to correct the shape of the orbitals in either case. In our *ab initio* molecular dynamics of ethylene we have used the GVB-occupation-averaged (GVB-OA) orbitals [32], but in benchmark calculations we have used the simpler Hartree–Fock-occupation-averaged (HF-OA) orbitals (with high spin coupling) [33]. In either case, the set of reference configurations from which single excitations are drawn in the subsequent CI expansion is of the complete active space (CAS) type, allowing all possible configurations of the active electrons in the occupation-averaged orbitals that are consistent with the Pauli exclusion principle. We refer to this form of wavefunction as HF-OA-CAS(n/m)*S or GVB-OA-CAS(n/m)*S, where n and m denote the number of electrons and orbitals in the active space which defines the reference configurations. The S indicates that single excitations are taken from the CAS(n/m) reference configurations.

The accuracy of the potential energy surfaces is determined also by the size of the electronic basis set. We have used double-ζ quality basis sets, which are the minimum that can be expected to describe both ground and excited

electronic states. For small organic molecules near their equilibrium configuration, one often finds Rydberg states among the low-lying excited electronic states. This implies that the inclusion of Rydberg basis functions would be desirable. At present, computational considerations render this impractical for quantum *ab initio* molecular dynamics. However, one can assess the accuracy of the dynamics using benchmark calculations and large basis sets. In Section III.B, we discuss the accuracy of the electronic wavefunction ansatz and remark on the importance of valence-Rydberg mixing (and its neglect in the dynamical calculations).

A final electronic structure issue is the nonadiabatic coupling between electronic states. The form of the coupling depends on whether an adiabatic or diabatic representation has been chosen. The adiabatic representation diagonalizes the electronic potential energy, while the diabatic representation minimizes the change in electronic character due to the nuclear perturbations and hence approximately diagonalizes the nuclear kinetic energy. The diabatic representation leads to smoother potential energy surfaces, and it is therefore often the preferred representation for time-dependent studies (i.e., molecular dynamics). However, without information about the electronic wavefunction at different geometries it is difficult to obtain a unique and path-independent set of diabatic states [34,35]. Hence, we (and others) prefer to use the unique adiabatic electronic states, in which case the form of the interstate coupling is

$$(\mathbf{d}^{IJ}) = \langle \phi_I(\mathbf{r};\mathbf{R}) | \frac{\partial}{\partial \mathbf{R}} | \phi_J(\mathbf{r};\mathbf{R}) \rangle_{\mathbf{r}} \tag{2.4}$$

In Eq. (2.4) the parametric dependence of the electronic wavefunction on the nuclear coordinates ($\mathbf{R}$) is denoted by the semicolon, and the integration is only over the electronic coordinates ($\mathbf{r}$). For our wavefunction ansatz, both the orbitals and the CI coefficients depend on the nuclear geometry and therefore both contribute to the derivative in Eq. (2.4). Because the orbitals are (state or occupation) averaged, the contribution from the CI coefficients is usually dominant [36,37] and consequently we have neglected the orbital contribution to the nonadiabatic coupling. Currently, we find the derivatives of the CI coefficients using numerical differentiation, but the required theory for analytic evaluation has been published [25]. In either case (numerical or analytic) the evaluation of the nonadiabatic coupling requires some care because one needs to ensure continuity. This can only be achieved if a consistent phase convention is adopted with respect to the electronic wavefunction. Failure to ensure this results in a wildly oscillating nonadiabatic coupling function.

B. Adaptive Time-Dependent Nuclear Basis Set

The AIMS method treats both the electrons and the nuclei quantum mechanically. The previous section dealt with the quantum nature of the electrons, and here we

discuss our strategy for incorporating nuclear quantum effects—the full multiple spawning (FMS) method that forms the nuclear dynamics component of AIMS. Quantum mechanical effects of the nuclei are necessary for proper modeling of photochemical processes because the excited-state lifetime of the molecule is usually short, and its (radiationless) decay back to the ground electronic state is often mediated by conical intersections—points of true degeneracy between two electronic states. Implicit in classical mechanics is the assumption that a single potential energy surface governs the dynamics. Hence, multielectronic state dynamics cannot be described using classical mechanics. At least formally, quantum mechanics can treat multielectronic states straightforwardly.

Within the context of traditional quantum chemistry, the interface between a quantum mechanical treatment of the electrons and the nuclei is quite problematic because the locality of quantum chemistry conflicts with the global nature of the nuclear Schrödinger equation. In principle, quantum nuclear dynamics requires the entire PES at each time step, but quantum chemistry only provides local information—given a nuclear geometry, it can return the potential and its derivatives. This immediate conflict imposes a stringent limitation on the method for the nuclear dynamics—compatibility with conventional quantum chemistry requires some form of localization of the nuclear Schrödinger equation. Furthermore, given the computational expense of quantum chemistry, the more local the method, the better; that is, at each time step we wish to require as few as possible PES and gradient evaluations. The complete locality of classical mechanics represents the ideal in this regard, leading us to develop a method that retains a classical flavor, reducing to pure classical mechanics in one limit, while allowing for quantum effects and converging to exact numerical solution of the Schrödinger equation in another limit.

The multiple-spawning method solves the nuclear Schrödinger equation using an adaptive time-dependent basis set that is generated using classical mechanics [38–41]. Individual basis functions are of the frozen Gaussian form. In the mid-1970s, Heller [42] pioneered the "frozen Gaussian approximation" (FGA); since that time, Gaussian wavepacket methods, along with Fourier methods [43–45], played a key role in popularizing time-dependent approaches to the nuclear Schrödinger equation. Gaussian wavepacket methods have successfully described a number of short time processes (see, for example, the original work of Heller and co-workers [46–49] as well as more recent publications [50–56]). Unlike the original FGA method, we take full account of the nonorthogonal nature of Gaussian basis sets by inverting the time-dependent overlap matrix at each time step and coupling the complex coefficients of the nuclear basis functions. The multiconfigurational nuclear wavefunction we use is of the form

$$\Psi = \sum_j \chi_j(\mathbf{R}; t)\phi_j(\mathbf{r}; \mathbf{R}) \tag{2.5}$$

where the index I denotes the electronic state, $\phi_I(\mathbf{r};\mathbf{R})$ is an electronic wavefunction (which is allowed to depend parametrically on the nuclear coordinates), and $\chi_I(\mathbf{R};t)$ is the time-dependent nuclear wavefunction associated with the Ith electronic state. An arbitrary number of electronic states and nuclear degrees of freedom is permitted in Eq. (2.5), and we use bold letters to denote vectors or matrices. Unlike mean-field based methods [57–60], the AIMS wavefunction ansatz associates a unique nuclear wavefunction with each electronic state, thereby allowing for qualitatively different nuclear dynamics on different electronic states (e.g., bound vs. dissociative). The nuclear wavefunction on each electronic state is represented as a superposition of multidimensional traveling frozen Gaussian basis functions with time-dependent coefficients:

$$\chi_I(\mathbf{R};t) = \sum_{j=1}^{N_I(t)} C_j^I(t)\chi_j^I(\mathbf{R};\bar{\mathbf{R}}_j^I(t),\bar{\mathbf{P}}_j^I(t),\bar{\gamma}_j^I(t),\boldsymbol{\alpha}_j^I) \tag{2.6}$$

where the index j labels nuclear basis functions on electronic state I, $N_I(t)$ is the number of nuclear basis functions on electronic state I at time t (this number is allowed to change during the propagation), and we have explicitly denoted the time-dependent parameters of the individual basis functions. Individual, multidimensional, nuclear basis functions are expressed as a product of one-dimensional Gaussian basis functions

$$\chi_j^I(\mathbf{R};\bar{\mathbf{R}}_j^I(t),\bar{\mathbf{P}}_j^I(t),\bar{\gamma}_j^I(t),\boldsymbol{\alpha}_j^I) = e^{i\bar{\gamma}_j^I(t)t}\prod_{\rho=1}^{3N}\chi_{\rho_j}^I(R;\bar{R}_{\rho_j}^I(t),\bar{P}_{\rho_j}^I(t),\alpha_{\rho_j}^I) \tag{2.7a}$$

$$\chi_{\rho_j}^I(R;\bar{R}_{\rho_j}^I(t),\bar{P}_{\rho_j}^I(t),\alpha_{\rho_j}^I) = \left(\frac{2\alpha_{\rho_j}^I}{\pi}\right)^{1/4}\prod_{\rho=1}^{3N}\exp[-\alpha_{\rho_j}^I(R_{\rho_j}-\bar{R}_{\rho_j}^I(t))^2 + i\bar{P}_{\rho_j}^I(t)(R_{\rho_j}-\bar{R}_{\rho_j}^I(t))] \tag{2.7b}$$

where the index ρ enumerates the 3N coordinates of the molecule, typically chosen to be Cartesian coordinates. The frozen Gaussian basis functions are parameterized with a time-independent width ($\alpha_{\rho_j}^I$) and time-dependent position, momentum, and nuclear phase [$\bar{R}_{\rho_j}^I(t)$, $\bar{P}_{\rho_j}^I(t)$, $\bar{\gamma}_j^I(t)$, respectively]. We have chosen to propagate the time-dependent position and momentum parameters using Hamilton's equations of motion

$$\begin{aligned}\frac{\partial\bar{R}_{\rho_j}^I}{\partial t} &= \frac{\bar{P}_{\rho_j}^I}{m_\rho}\\ \frac{\partial\bar{P}_{\rho_j}^I}{\partial t} &= -\left.\frac{\partial V_H(\mathbf{R})}{\partial R_{\rho_j}}\right|_{\bar{R}_{\rho_j}^I(t)}\end{aligned} \tag{2.8}$$

and the nuclear phase is propagated according to the usual semiclassical prescription—that is, as the integral of the Lagrangian:

$$\frac{\partial \bar{\gamma}_j^I}{\partial t} = -V_{II}(\bar{\mathbf{R}}_j^I(t)) + \sum_{\rho=1}^{3N} \frac{(\bar{P}_{\rho_j}^I(t))^2}{2m_\rho} \tag{2.9}$$

In Eqs. (2.8) and (2.9), $V_{II}(\mathbf{R})$ is the potential energy of the Ith electronic state, and m_ρ is the mass of the ρth degree of freedom.

Implicit in the choice of classical propagator for the position and momentum parameters is the assumption that classical mechanics provides a reasonable description, on average, of the quantum dynamics. In favorable cases, a relatively small number of nuclear basis functions may be required to obtain an accurate description of the wavefunction. However, one must realize that this will not always be true, leading one to consider means of incorporating quantum effects directly into the time-dependence of the nuclear basis function parameters. One such alternative propagates the position and momentum parameters using a time-dependent variational principle (TDVP) [61,62], but we find this choice less desirable for two reasons. The first is conceptual: such a variational propagator does not reduce to the well-understood classical limit in the extreme case of a single nuclear basis function. The second reason is practical: A variational propagator requires the calculation of more matrix elements and their derivatives than otherwise required. This conflicts with the locality of quantum chemistry and is thus undesirable for *ab initio* quantum nuclear dynamics. Numerical considerations also guide the use of a fixed width parameter ($\alpha_{\rho_j}^I$): Propagation of this parameter requires the calculation of second derivatives of the potential energy surfaces which can be extremely tedious if the PESs are determined by direct solution of the electronic Schrödinger equation. It is reasonable to assume that these two choices result in a penalty: Compared to fully variational treatment of a Gaussian basis set [55,63,64], we will require a larger nuclear basis set to achieve numerical convergence. The finite size of the nuclear basis set is the first approximation we make; and, as usual, larger basis sets generally lead to improved results. The issue of basis set size and convergence is discussed in more detail in Section III.B. Here we only note that at each point in time the size of the nuclear basis set ($N_{\text{nuc}}(t)$) is given by the sum of nuclear basis functions on all electronic states included in the calculation:

$$N_{\text{nuc}}(t) = \sum_I N_I(t) \tag{2.10}$$

In general, the optimal choice for the time-independent width is not known *a priori* (the only exception is a separable harmonic PES with one nuclear basis

function in which case [42] $\alpha^I_{\rho_j} = m_\rho \omega^I_\rho/2$, where ω^I_ρ is the harmonic vibrational frequency of the ρth coordinate on electronic state I). We have always chosen the width to be independent of both the electronic state index and the nuclear basis function index (i.e., $\alpha^I_{\rho_j} = \alpha_\rho$ for all I and j). Specific values were chosen by requiring the results to be stable with respect to the width of the basis functions. Our experience is that as long as the basis functions are not very wide, the results are relatively independent of the precise choice of the width parameters. Nevertheless, since they are chosen empirically, we must view them as parameters that characterize the nuclear basis set.

A set of coupled equations for the evolution of the basis function coefficients is obtained by substituting the wavefunction ansatz of Eqs. (2.5)–(2.7) into the nuclear Schrödinger equation

$$\frac{d\mathbf{C}^I(t)}{dt} = -i(\mathbf{S}_{II}^{-1})\left\{[\mathbf{H}_{II} - i\dot{\mathbf{S}}_{II}]\mathbf{C}^I + \sum_{J\neq I}\mathbf{H}_{IJ}\mathbf{C}^J\right\} \tag{2.11}$$

For compactness and clarity, Eq. (2.11) is written in matrix notation. It is similar to the more familiar case of a time-independent basis set expansion but with two important differences: The AIMS basis is time-dependent and nonorthogonal. As a consequence, the proper propagation of the coefficients requires the inverse of the (time-dependent) nuclear overlap matrix

$$(S_{II})_{kl} = \langle \chi^I_k | \chi^I_l \rangle_{\mathbf{R}} \tag{2.12}$$

as well as its right acting time derivative

$$(\dot{S}_{II})_{kl} = \left\langle \chi^I_k \middle| \frac{\partial}{\partial t}\chi^I_l \right\rangle_{\mathbf{R}} \tag{2.13}$$

Both of these matrix elements are readily computed analytically (the subscript **R** denotes integration over the nuclear coordinates and by definition $\mathbf{S}_{IJ}$ and $\dot{\mathbf{S}}_{IJ}$ vanish for $I \neq J$). In Eq. (2.11), $\mathbf{H}_{IJ}$ is the full Hamiltonian matrix including both electronic and nuclear terms. Each matrix element of **H** is written as the sum of the nuclear kinetic energy ($\hat{T}_{\mathbf{R}}$) and the electronic Hamiltonian ($\hat{H}_e$)

$$H_{IkJk'} = \langle \chi^I_k \phi_I | \hat{H}_e + \hat{T}_{\mathbf{R}} | \phi_J \chi^J_{k'} \rangle \tag{2.14}$$

and the integration is over both the electronic and nuclear coordinates. The electronic Hamiltonian includes all of the Coulomb interactions as well as the electronic kinetic energy

$$\langle \chi^I_k \phi_I | \hat{H}_e | \phi_J \chi^J_{k'} \rangle = \langle \chi^I_k | H^e_{IJ} | \chi^J_{k'} \rangle + 2D_{IkJk'} + G_{IkJk'} \tag{2.15}$$

where

$$H_{IJ}^{e} = \langle \phi_I | H_e | \phi_J \rangle_{\mathbf{r}} \tag{2.16a}$$

$$D_{Ik,Jk'} = \langle \chi_k^I | \sum_{\rho=1}^{3N} d_\rho^{IJ} \frac{1}{2m_\rho} \frac{\partial}{\partial R_\rho} | \chi_{k'}^J \rangle \tag{2.16b}$$

$$G_{Ik,Jk'} = \langle \chi_k^I | \sum_{\rho=1}^{3N} \frac{1}{2m_\rho} \langle \phi_I | \frac{\partial^2}{\partial R_\rho^2} | \phi_J \rangle | \chi_{k'}^J \rangle \tag{2.16c}$$

In the previous section, we discussed the calculation of the PESs needed in Eq. (2.16a) as well as the nonadiabatic coupling terms of Eqs. (2.16b) and (2.16c). We have noted that in the diabatic representation the off-diagonal elements of Eq. (2.16a) are responsible for the coupling between electronic states while D_{IJ} and G_{IJ} vanish. In the adiabatic representation the opposite is true: The off-diagonal elements of Eq. (2.16a) vanish while D_{IJ} and G_{IJ} do not. In this representation, our calculation of the nonadiabatic coupling is approximate because we assume that G_{IJ} is negligible and we make an approximation in the calculation of D_{IJ}. (See end of Section II.A for more details.)

The obstacle to simultaneous quantum chemistry and quantum nuclear dynamics is apparent in Eqs. (2.16a)–(2.16c). At each time step, the propagation of the complex coefficients, Eq. (2.11), requires the calculation of diagonal and off-diagonal matrix elements of the Hamiltonian. These matrix elements are to be calculated for each pair of nuclear basis functions. In the case of *ab initio* quantum dynamics, the potential energy surfaces are known only locally, and therefore the calculation of these matrix elements (even for a single pair of basis functions) poses a numerical difficulty, and severe approximations have to be made. These approximations are discussed in detail in Section II.D. In the case of analytic PESs it is sometimes possible to evaluate these multidimensional integrals analytically. In either case (analytic or *ab initio*) the matrix elements of the nuclear kinetic energy

$$\langle \chi_k^I | \hat{T}_{nuc} | \chi_{k'}^J \rangle = \langle \chi_k^I | \sum_{\rho=1}^{3N} \frac{\hat{v}^2}{2m_\rho \partial R_\rho^2} | \chi_{k'}^J \rangle \delta_{IJ} \tag{2.17}$$

are computed analytically.

C. Selection of Initial Conditions, Propagation, and Spawning

From the very beginning we have emphasized that the AIMS method uses an adaptive basis set. This property is at the core of the AIMS method, and much of this subsection will be devoted to this topic. However, before we elaborate on it, we discuss the selection of initial conditions and some topics regarding the propagation.

A complete description of the method requires a procedure for selecting the initial conditions. At $t = 0$, initial values for the complex basis set coefficients and the parameters that define the nuclear basis set (position, momentum, and nuclear phase) must be provided. Typically at the beginning of the simulation only one electronic state is populated, and the wavefunction on this state is modeled as a sum over discrete trajectories. The size of initial basis set ($N_I(t = 0)$) is clearly important, and this point will be discussed later. Once the initial basis set size is chosen, the parameters of each nuclear basis function must be chosen. In most of our calculations, these parameters were drawn randomly from the appropriate Wigner distribution [65], but the earliest work used a quasi-classical procedure [39,66,67]. At this point, the complex amplitudes are determined by projection of the AIMS wavefunction on the target initial state ($\Psi_{t=0}^{\text{exact}}$)

$$C_k^I(0) = \sum_{k'=1}^{N_I(0)} S_{Ikk'}^{-1} \langle \chi_{k'}^I(t = 0) | \Psi_{t=0}^{\text{exact}} \rangle \tag{2.18}$$

We have used various integrators (e.g., Runga–Kutta, velocity verlet, midpoint) to propagate the coupled set of first-order differential equations: Eqs. (2.8) and (2.9) for the parameters of the Gaussian basis functions and Eq. (2.11) for the complex amplitudes. The specific choice is guided by the complexity of the problem and/or the stiffness of the differential equations.

As the calculation progresses, the size of the basis set is adjusted in a physically motivated way. This basis set expansion is aimed only at describing quantum mechanical effects associated with electronic nonadiabaticity and *not* at correcting the underlying classical dynamics of individual nuclear basis functions. Hence, a new basis function may be spawned whenever an existing basis function passes through a region of significant electronic coupling to another electronic state. In general, the new function is spawned on a different electronic state than the existing basis function that generates it. More recently we have allowed for spawning on the same electronic state—for example, to allow for tunneling effects—and this extension is discussed in Section II.F. By allowing the basis set to grow only at specific regions (or instances), the growth of basis set size with time can be controlled. Although one can envision cases where the basis set size grows to an unmanageable level, so far this has rarely been a problem in practice because nonadiabatic events are very short in most chemical problems and often infrequent. The practical implementation of the spawning algorithm that expands the basis set is as follows. First, we define two parameters λ_0 and λ_f that signal when a region of nonadiabatic coupling has been entered and exited, respectively. (The values of these parameters are chosen by running test calculations and monitoring the magnitude of an effective nonadiabatic coupling; see below.) At each time step and for each

nuclear basis function in the wavepacket, we calculate an effective (dimensionless) coupling

$$\Lambda_{IJ}^{\text{eff}} = \begin{cases} \left| \frac{V_{IJ}(\mathbf{R})}{V_{II}(\mathbf{R}) - V_{JJ}(\mathbf{R})} \right|, & \text{diabatic} \\ |\dot{\mathbf{R}} \cdot \mathbf{d}_{IJ}|, & \text{adiabatic} \end{cases} \tag{2.19}$$

where the overdot indicates the time derivative. If the value of $\Lambda_{IJ}^{\text{eff}}$ at a given time step (and for a particular basis function) is larger than the parameter λ_0, this signals that a region of significant electronic coupling has been entered, and that basis function has the opportunity to spawn a new basis function(s). This point in time is labeled t_0. The parent basis function is now propagated forward in time according to Hamilton's equations of motion. This propagation is uncoupled from the propagation of the wavepacket; that is, we do not propagate the complex amplitudes of Eq. (2.11). We stop the uncoupled propagation when the magnitude of $\Lambda_{IJ}^{\text{eff}}$ drops below λ_f because this indicates that the region of nonadiabatic coupling has ended. This time is labeled t_f. Within this region of electronic coupling ($t_f - t_0$), a predetermined number of basis functions may be spawned and we label this parameter MULTISPAWN. The first basis function is spawned at the point in time in which $\Lambda_{IJ}^{\text{eff}}$ reaches its maximum value (this time is labeled $t_{\max}$), and the rest of the basis functions are spread out evenly in time before and after $t_{\max}$. For example, if MULTISPAWN = 3, one basis function is spawned at $t_0 + 0.5(t_{\max} - t_0)$, a second at $t_{\max}$, and a third at $t_{\max} + 0.5(t_f - t_{\max})$.

A pictorial description of the spawning algorithm is given in Fig. 1 using a collinear A + BC → AB + C reaction. The upper and lower set of panels correspond to two diabatic potential energy surfaces (represented by contour lines), correlating to A + BC and AB + C respectively. The two diabatic surfaces are coupled via a constant potential energy term, and they are plotted in Jacobi coordinates: the A to BC center-of-mass distance, R, and the BC distance, r. The nuclear wavefunctions are superimposed on the contour lines. The calculation begins with population on a single diabatic PES, uppermost left panel. As the basis functions approach the nonadiabatic region, new basis functions are created (i.e., "spawned") on the other diabatic state. The locations of individual basis functions are indicated by the triangles. Initially (middle panels), the parent basis functions overlap the ones they spawned yet the subsequent dynamics (right panels) are very different: the parent wavefunction corresponds to an A+BC arrangement and the spawned wavefunction to an AB+C arrangement.

The immediate question is where (in phase space) to place the newly spawned basis functions. The optimal choice will maximize the absolute value of the coupling matrix element between the existing basis function (i.e., the

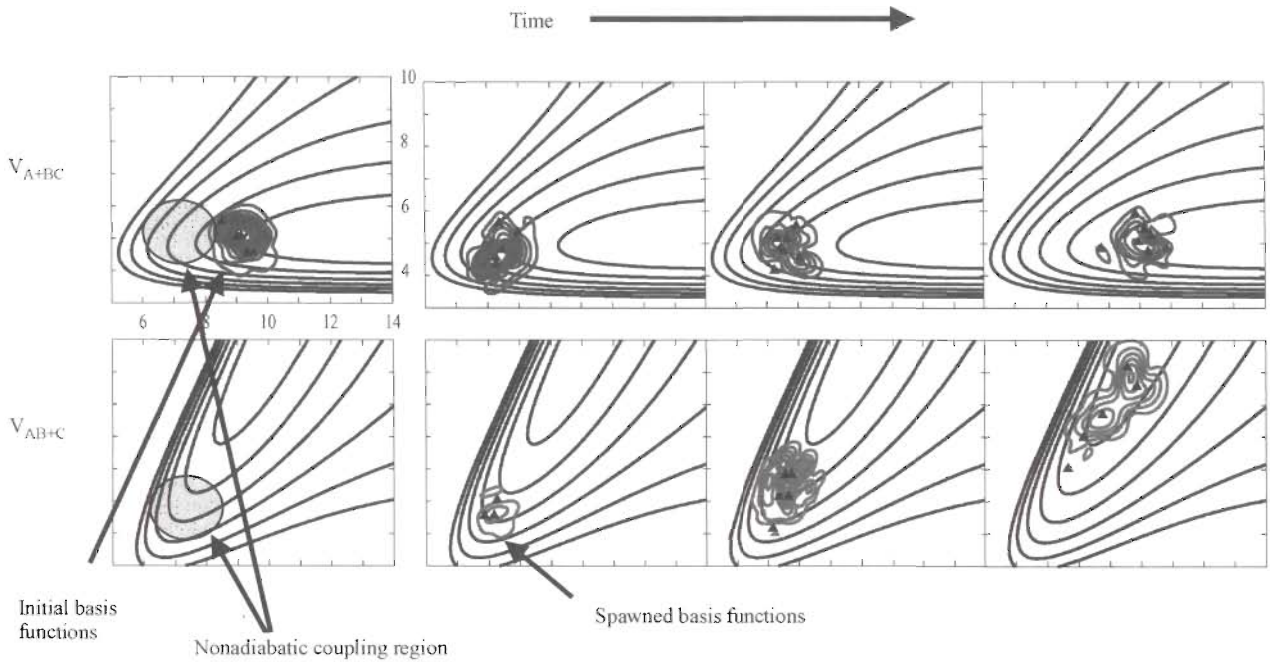

Figure 1. Schematic illustration of the spawning algorithm for a collinear A + BC → AB + C reaction. The top and bottom panels correspond to two diabatic potential energy surfaces, correlating to A + BC and AB + C, respectively. The potential energy surfaces are represented in Jacobi coordinates (the A to BC center-of-mass distance and the B–C distance). Superimposed on the PESs are the nuclear wavefunctions in the diabatic representation. The calculation begins with population on a single diabatic potential energy surface (upper left panel); and as basis functions traverse the nonadiabatic region (roughly indicated by the shaded circle), new basis functions are created on the other diabatic state (second, third, and fourth lower panels). The locations of individual Gaussian basis functions are indicated by the triangles. (Figure adapted from Ref. 40.)

parent) and the newly spawned basis function: $|\langle\chi_k^I|H_{IJ}|\chi_{k'}^J\rangle|$. The connection with classical mechanics suggests also requiring that the classical energy of the spawned basis function be the same as its parent. This requirement is in direct contradiction with short-time first-order perturbation theory analysis that predicts that the spawned function should be proportional to the parent basis function multiplied by the nonadiabatic coupling function. Hence, for example in the case of constant nonadiabatic coupling, first-order perturbation theory predicts that the spawned basis function will have the same momentum and position as its parent (and therefore a different classical energy whenever the parent basis function does not lie exactly at either the crossing seam of the diabats or a conical intersection in the adiabatic representation). Nevertheless, the equal energy constraint is justified from a long-time analysis (e.g., through the state-to-state form of Fermi's Golden Rule [68]), and one may therefore expect the expectation value of the energy (in an exact quantum mechanical calculation) to smoothly interpolate from the short-time (first-order perturbation theory) limit to the long-time limit. Figure 2 demonstrates this for a simple (yet realistic) case of a one-dimensional avoided crossing model. In this example, only one electronic state is populated at time zero; but as the wavepacket traverses the nonadiabatic region, it bifurcates and a new component is generated on the other electronic state. Apart from a phase relation, these two components propagate separately. After the two components of the wavepacket have left the region of nonadiabatic coupling, the expectation value of the energy can be defined for each electronic state individually; that is, there are no interference terms between the wavepackets on each electronic state:

$$\begin{aligned}\langle\Psi(\mathbf{R};t)|\hat{H}|\Psi(\mathbf{R};t)\rangle = {} & N_1(t)\langle\chi_1(\mathbf{R};t)|H_{11}|\chi_1(\mathbf{R};t)\rangle \\ & + N_2(t)\langle\chi_2(\mathbf{R};t)|H_{22}|\chi_2(\mathbf{R};t)\rangle \end{aligned} \tag{2.20}$$

The energy-conserving nature of the transition (which is strictly valid only in the limit that the nonadiabatic coupling region is traversed infinitely slowly) implies that each of these energy expectation values be the same, where we stress that the above expression and the preceding statement are only valid outside of the nonadiabatic coupling region. Classically, the equality of these two quantum mechanical expectation values implies that the average energy of the basis functions representing the wavepacket on each electronic state should be the same. Because the phase space centers of the basis functions follow Hamilton's equations, it is necessarily true that the classical energy chosen for the spawned basis function will be conserved throughout the propagation. Therefore, the proper asymptotic mean energy should be imposed at the time of spawning, and the requirement of equality between the average classical energy of the wavepackets on different electronic states is met by requiring the

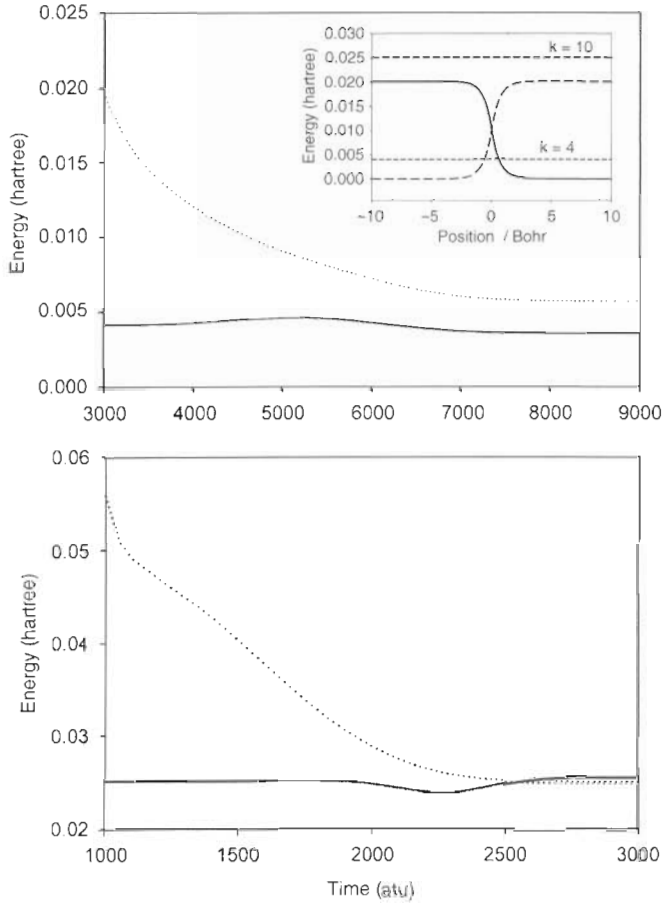

Figure 2. Expectation value of energy as a function of time (in atomic units) on the ground and excited electronic states for Tully's simple one-dimensional avoided crossing model [96]. The inset in the upper panel depicts the two diabatic states, indicated by full and dashed lines. Initially only one electronic state (dashed line) is populated and the wavepacket is a Gaussian centered at $x = -10$ bohr with a width of 0.5 bohr^{-2}. As the wavepacket traverses the nonadiabatic region, population is transferred to the other (full line) electronic state. The horizontal lines in the inset indicate the energy of the wavepacket for the two cases shown in the upper and lower panels. Long dashed line: the wavevector $k = 10$, yielding sufficient energy to populate both electronic states asymptotically. Short dashed line: the wavevector $k = 4$, yielding insufficient energy to cross the barrier on the ground adiabatic state (not shown). In both panels, the full line denotes the expectation value of the energy of the initially populated state, and the dotted one denotes this expectation value on the newly populated state. Upper panel: $k = 4$; lower panel: $k = 10$. In both cases, the expectation value of energy on the newly populated state (dotted line) starts as predicted by short-time first-order perturbation theory, but at the end of the nonadiabatic event it is nearly energy-conserving as would be predicted for an infinitely long nonadiabatic event. The mass used is 2000 atomic units, similar to the mass of a hydrogen atom.

parent and spawned basis functions to have the same classical energy. We reemphasize at this point that the Schrödinger equation is solved for the time-dependent coefficients of all basis functions. Therefore, our only duty is to justify that the restricted variational space we sample with the spawning procedure indeed covers the physically relevant space. To the extent that we sample only what is necessary, computational efficiency will be optimal. However, if the spawned functions under-sample the relevant Hilbert space, the accuracy of the method will suffer.

When we include the constraint that the newly spawned basis function will have the same classical energy as the parent basis function, we have an over-complete set of equations:

$$\begin{aligned}
&\frac{\partial}{\partial \bar{R}^J_{\rho k'}} \langle \chi^I_k | H_{IJ} | \chi^J_{k'} \rangle = 0, \qquad \rho = 1, \ldots, 3N \\
&\frac{\partial}{\partial \bar{P}^J_{\rho k'}} \langle \chi^I_k | H_{IJ} | \chi^J_{k'} \rangle = 0, \qquad \rho = 1, \ldots, 3N \\
&V_{II}(\bar{\mathbf{R}}^I_k) + \sum_{\rho=1}^{3N} \frac{\bar{P}^{I\,2}_k}{2m_\rho} = V_{JJ}(\bar{\mathbf{R}}^J_{k'}) + \sum_{\rho=1}^{3N} \frac{\bar{P}^{J\,2}_{\rho k'}}{2m_\rho}
\end{aligned} \tag{2.21}$$

These equations can be solved in a least-squares sense, but in general they do not have a unique solution. The finite phase space width of the basis functions tends to dampen the sensitivity of the results, especially branching ratios, to the particular solution that is chosen. This sensitivity is further reduced when convergence with respect to MULTISPAWN is demonstrated.

Nevertheless, it is instructive to consider the simplest solutions that arise in a concrete example. Assuming two diabatic states in one dimension with a constant interstate coupling, maximizing the Hamiltonian coupling matrix element is equivalent to maximizing an overlap integral. This integral has the form of a product of two Gaussian functions whose arguments are the differences in momentum and position between the parent and spawned basis function. Two simple approximate solutions are "position-preserving" and "momentum-preserving" spawns, where the spawned basis function is placed at either the same position or momentum as its parent. The conjugate variable must then be adjusted to satisfy the constraint equation. In a one-dimensional problem, there is no ambiguity concerning the adjustment made to the conjugate variable, and the position-preserving spawn gives rise to exactly the momentum adjustment which Tully has used in the surface hopping method [69] and which was later justified by Herman via a semiclassical argument [70]. Interestingly, the second type of solution, the momentum-preserving spawn, can give rise to

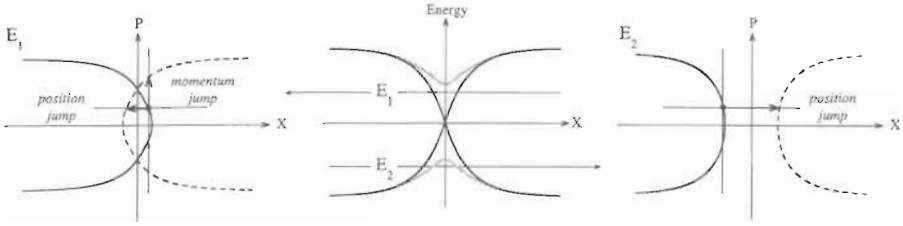

Figure 3. Schematic illustration of position- and momentum-preserving spawns for the one-dimensional avoided crossing model of Fig. 2. The two diabatic (black) and adiabatic (gray) potentials are depicted in the middle panel, and the two horizontal lines indicate the energies of the trajectories shown on the right and left panels, E_2 and E_1, respectively. Left panel: Phase space plot of a diabatic trajectory at energy E_1 that is above the ground-state adiabatic barrier. The full line indicates the trajectory traversed by the populated basis function, and the dashed line indicates the trajectory traversed by the unpopulated basis function (at the same energy E_1). The horizontal and perpendicular arrows show momentum- and position-preserving spawns where the spawned basis function is placed at either the same momentum or position as its parent. Right panel: Same as left panel but for energy E_2 that is below the ground-state adiabatic barrier. At energies below the adiabatic barrier, only momentum-preserving spawns are possible. For this specific example, the momentum-preserving spawn describes tunneling. (Figure adapted from Ref. 40.)

tunneling effects as demonstrated in Fig. 3. The two types of spawns for a simple one-dimensional avoided crossing model are depicted in this figure. Note that at energies below the adiabatic barrier (rightmost panel in Fig. 3), there is no solution corresponding to a position-preserving spawn, and the momentum-preserving spawn describes tunneling. However, this is a very special type of tunneling, contingent on the multielectronic state representation of the problem. For example, in the model shown in Fig. 3, both types of spawns are forbidden if the adiabatic representation of the electronic states is used.

We have obtained further empirical information on the optimal choice of the position and momentum of the new basis function by studying the Wigner transform of the wavepacket calculations. In Fig. 4 we show snapshots of the ground- (black contours) and excited-state (gray contours) Wigner distributions for the one-dimensional problem of Figs. 2 and 3. The distributions are shown at three instances of time, namely, the onset of population transfer (left panels), the peak of population transfer (middle panels), and long after the population transfer is completed (right panels). The upper and lower set of panels are for relative kinetic energies corresponding to wavevectors of $k = 4$ and 10, respectively (see inset in upper panel of Fig. 2.) Along with the Wigner distributions, we plot the expectation value of position versus momentum for the wavepacket traveling on the initially populated electronic state (black line), a mirror image of this path (gray line), and the actual expectation value of the position versus

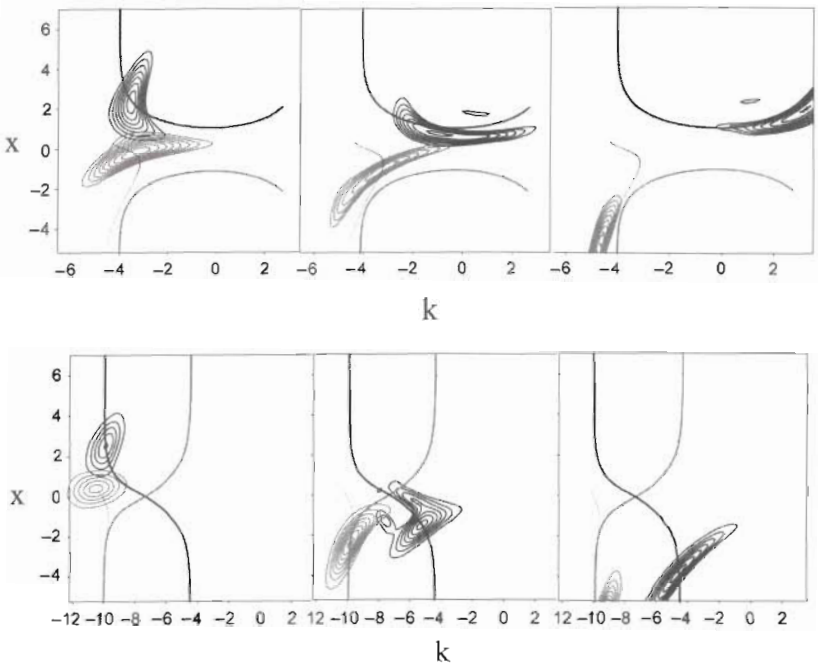

Figure 4. Phase space evolution of Wigner distributions for the two-state, one-dimensional model of Figs. 2 and 3. The upper and lower panels are for different initial relative kinetic energies (k = 4 and 10, respectively; see inset in upper panel of Fig. 2). The black and gray contour lines denote the Wigner distributions (computed using the exact quantum mechanical wavefunction) on the initially and newly populated electronic states, respectively. In all panels, the thick black line denotes the expectation value (position vs. momentum for the entire simulation) of the wavefunction on the initially populated state, and the thick gray line is a mirror image of the thick black line, analogous to Fig. 3. The dotted line is the actual expectation value (position vs. momentum for the entire simulation) on the newly populated state. In both the upper and lower panels, snapshots of the Wigner distributions are shown at the onset of the nonadiabatic event (left panels), the peak of the nonadiabatic event (middle panels), and immediately after the completion of the nonadiabatic event (right panels). For clarity, the population on each state has been scaled to unity prior to calculating the Wigner transform and therefore the contours do not reflect the population of the states. At low energy (upper set of panels) the nonadiabatic event is not well-described in terms of the idealized limit of position- and/or momentum-preserving spawns. The event begins with a momentum-preserving (i.e., position-jump) population transfer (left panel) and continues with a mixture of position- and momentum-preserving population transfer (middle panel). After the nonadiabatic event is completed (right panel), the expectation value of position and momentum on the newly populated state (dotted line) is similar (but not identical) to that of the idealized spawned trajectory (gray line). Lower set of panels: Same as above, but for an energy that is above the barrier on the ground adiabatic state. Here, the actual expectation values of position and momentum on the newly populated state (dotted line) do coincide with those of the idealized spawned trajectory (gray line) and the position-preserving nature of the "spawn" is evident in the middle panel.

momentum on the newly populated state (dotted line). This figure demonstrates a few points. First, in both cases (upper and lower panels) the population transfer begins with a momentum preserving event (leftmost panel). Second, the peak of the nonadiabatic event is characterized by a mixture of position- and momentum-preserving "spawns." Third, when the nonadiabatic event is completed, the mirror phase space path (gray line) is either an excellent (lower right panel) or reasonable (upper right panel) approximation to the exact path of the wavepacket (dotted line).

In practice we take the position-preserving spawn, and the momentum of the new basis function is calculated by

$$\mathbf{P}_{\text{new}} = \mathbf{P}_{\text{old}} - D\hat{\mathbf{h}}_{IJ} \tag{2.22}$$

where $\hat{\mathbf{h}}$ is a unit vector along the nonadiabatic coupling direction

$$\hat{\mathbf{h}}_{IJ} = \frac{\mathbf{d}_{IJ}}{|\mathbf{d}_{IJ}|} \tag{2.23}$$

and D is a scalar variable whose value is determined by conservation of energy. In some cases, it may happen that the surface to which a spawn should occur is not classically energetically accessible, or that there is sufficient energy to spawn but there is not enough momentum along the direction used to adjust the energy during spawning. In these instances, we use a steepest descent quenching of the position-preserving spawn until the constraint equation is satisfied. In one dimension, this leads to a momentum-preserving spawn, but in multiple dimensions this can give rise to spawned functions that do not preserve either position or momentum.

Certain additional numerical considerations should be satisfied before a spawning attempt is successful. First, in order to avoid unnecessary basis set expansion, we require that the parent of a spawned basis function have a population greater than or equal to P_{min}, where the population of the kth basis function on electronic state I is defined as

$$p_k^I = \left|C_k^I\right|^2 \tag{2.24}$$

This threshold prevents basis functions with small population (which are only negligibly contributing to the nuclear wavefunction in any case) from giving rise to new basis functions. The ideal of $P_{\text{min}} = 0$ is usually computationally wasteful, leading to many unpopulated basis functions. However, it is also important to note that the uncertainty in branching ratios incurred by finite P_{min} is dependent on the average population of a basis function in the wavepacket. Second, it

is pointless to create new basis functions that are redundant with existing basis functions. We therefore enforce a maximum overlap, S_{max}, that any new basis function is allowed to have with any existing basis function in the wavepacket. Any potentially newly spawned basis function that has been back-propagated to t_0 and has an overlap greater than S_{max} with any other basis function on the same electronic state in the same wavepacket at time t_0 is not spawned. Finally, we note that we do allow for back-spawning; that is, a newly spawned basis function on a given electronic state is allowed to transfer population back to the other electronic state.

Once we have determined which basis functions will be spawned (and their initial positions and momenta), they are back-propagated in time to t_0, where they are added to the set of basis functions. The coupled propagation of all of the basis functions is then continued, beginning again from time t_0; that is, Eq. (2.11) is integrated again along with Hamilton's equations of motion. The final-state analysis of the results is discussed in Section II.D, following a review of various approximations that can, and often should, be made.

D. Approximations and Analysis of Results

So far, the only approximation in our description of the FMS method has been the use of a finite basis set. When we test for numerical convergence (small model systems and empirical PESs), we often do not make any other approximations; but for large systems and/or *ab initio*-determined PESs (AIMS), additional approximations have to be made. These approximations are discussed in this subsection in chronological order (i.e., we begin with the initial basis set and proceed with propagation and analysis of the results).

In Section II.C we discussed the selection of initial conditions for the nuclear basis set and its propagation. After selecting the position and momentum parameters for each nuclear basis function, the complex amplitudes were determined by a least-squares fitting procedure [cf. Eq. (2.18)] and then propagated simultaneously. If this procedure of coupled propagation is followed, then one is attempting a particular form of wavepacket propagation with classical mechanics as a guide for basis set selection, expansion (i.e., spawning), and propagation. In this mode, convergence to exact quantum mechanical results is ensured for a sufficiently large number of basis functions. When quantal aspects of the single-surface dynamics are important, this option should be used (as well as a coherent analysis of the final results). The first approximation in FMS (beyond the use of a finite basis set) assigns a unit initial amplitude to each of the initial basis functions and propagates each one independently; however, each basis function can spawn new basis functions in nonadiabatic regions, and these in turn can spawn additional basis functions, and these multiple descendents of a single parent are fully coupled (on all potential energy surfaces) by the FMS algorithm. This "independent-first-generation" (IFG) approximation

assumes that a properly chosen swarm of classical trajectories will suffice to describe the dynamics occurring on a single electronic state. While this approximation allows one to carry out a very complete sampling of initial-state phase space without introducing an unmanageable amount of coupling (between basis functions), it may not be sufficiently accurate when quantum interference effects on a single electronic state are important. In most of our AIMS calculations, we have used the IFG approximation because of computational limitations; but when predetermined PESs were available, we have usually preferred coupled propagation.

The next set of approximations concerns the propagator and the evaluation of the matrix elements that are required for Eq. (2.11). At each time step and for each nuclear basis function, numerical integration of Eq. (2.11) requires diagonal and off-diagonal terms of the Hamiltonian matrix elements ($\langle\chi_k^I|H_{II}^e|\chi_{k'}^I\rangle$ and $\langle\chi_k^I|H_{IJ}^e|\chi_{k'}^J\rangle$, respectively). The need to evaluate these integrals is the greatest drawback of the FMS method. Given an analytic representation of the PESs and their couplings, it is sometimes possible to evaluate these multidimensional integrals analytically; but when the PESs (and their couplings) are known only locally, as in AIMD and AIMS, this is not possible. By expanding the wavefunction in a (traveling) Gaussian basis set, we have localized individual components of the wavefunction and thus any integrals involving the semilocal nuclear basis functions. Motivated by this localization, we evaluate the required integrals using a first-order saddle-point (SP) approximation [71]:

$$\langle\chi_k^I|H_{IJ}^e|\chi_{k'}^J\rangle = H_{IJ}^e(\tilde{\mathbf{R}})\langle x_k^I|x_{k'}^J\rangle \tag{2.25}$$

where $\tilde{\mathbf{R}}$ is the location of the centroid of the product of the basis functions χ_k and $\chi_{k'}$. This approximation is applied to both diagonal ($I = J$) and off-diagonal ($I \neq J$) elements of the Hamiltonian, and it involves only the potential energy operator (the part involving kinetic-energy operator can be evaluated analytically for Gaussians basis functions). The SP approximation resembles the Mulliken–Ruedenberg and related approximations that have been used in electronic structure theory for the approximate evaluation of multicenter two-electron integrals [72]. This approximation has been tested for simple one-dimensional model problems [38,73,74] with favorable results. Nevertheless, it is a severe approximation whose quality should be tested more rigorously and, whenever possible, improved. Two obvious possible improvements involve the use of higher-order SP approximations—for example, second-order

$$\langle\chi_k^I|H_{IJ}^e|\chi_{k'}^J\rangle = H_{IJ}^e(\tilde{\mathbf{R}})\langle x_k^I|x_{k'}^J\rangle + \langle\chi_k^I|\mathbf{R}-\tilde{\mathbf{R}}|\chi_{k'}^J\rangle\frac{d}{d\mathbf{R}}H_{IJ}^e(\mathbf{R})\Big|_{\tilde{\mathbf{R}}} \tag{2.26}$$

or various forms of numerical quadrature. Although these approximations require more computational effort and are currently beyond our capabilities, they could greatly improve the accuracy of the integrals. A less obvious improvement, which does not require any additional calculations, is to incorporate more of the available information (about the PESs and their couplings) into the calculation of individual matrix elements. Although our knowledge of the PESs in AIMD is only local, it does increase with time. For example, for a single classical trajectory the potential and its derivative are only known at one point (geometry) at the first time step (assuming a simple first-order integrator). After n steps they are known at n geometries. In the AIMS method, we actually know the potential at many more points (geometries) at each instance of time. To see this, assume for simplicity that only one electronic state (I) is populated and that at time t there are $N_I(t)$ nuclear basis functions. In such a case, at time t the potential is known at $N_I(t)[N_I(t) + 1]/2$ points (geometries) even if we use the simple first-order SP approximation. As in the case of a classical propagation, this information grows linearly with time (even when the size of the nuclear basis set does not change). Equation (2.25) does not incorporate any of this additional information. Because the additional information (from other basis functions and from previous points in time) is irregular, it is not obvious how to incorporate (or weight) it. However, it is also obvious that not using it is quite wasteful, and future developments of the method should address this point. Our first attempt to exploit the temporal nonlocality of the Schrödinger equation is discussed in Section II.F.

The use of the SP approximation solves the problem of matrix element evaluation. Still, at each time step, $O(N^2_{\text{nuc}}(t))$ evaluations of potential energies and couplings are required. For *ab initio*-determined PESs, this can be quite tedious. Furthermore, the dynamics of the complex amplitude coefficients are governed by the Schrödinger equation even in the absence of intersurface coupling. Hence, the trajectory amplitudes will attempt to correct as much as possible the inadequacies of classical mechanics by exchanging population between trajectories with the same electronic state label. This behavior has no analog in classical mechanics, and it can obscure the classical interpretation of the results. In many cases this is desirable, but if the objective is to obtain a method that is "classical-like," then one should separate the dynamics occurring on single and multiple electronic states. By invoking the idea of operator splitting, this separation can be achieved and the number of potential energy evaluations can be further reduced. For a two-electronic-state problem we write the Hamiltonian operator as a sum of single-state (*SS*) and interstate (*IS*) terms:

$$\hat{H} = \hat{H}_{SS} + \hat{H}_{IS} = \begin{pmatrix} \hat{H}_{11} & \\ & \hat{H}_{22} \end{pmatrix} + \begin{pmatrix} & \hat{H}_{12} \\ \hat{H}_{21} & \end{pmatrix} \tag{2.27}$$

Invoking a Trotter factorization [75], we write the time evolution operator as

$$\exp(-i\hat{H}t) \approx \exp(-i\hat{H}_{SS}t/2)\exp(-i\hat{H}_{IS})\exp(-i\hat{H}_{SS}t/2) \tag{2.28}$$

The nonclassical evolution of the trajectory amplitudes can now be avoided by forbidding the interaction of basis functions during the single-surface propagation. This is accomplished by substituting the frozen Gaussian propagator [46] for $\exp(-i\hat{H}_{ss}t/2)$. At each time step, Eq. (2.28) with the frozen Gaussian propagator requires only $N_{\text{nuc}}(t)$ PES evaluations, whereas a coupled single-state propagation requires

$$\sum_{I=1}^{N\text{ states}} N_I(t)[N_I(t)+1]/2 = 1/2\left[N_{\text{nuc}}(t) + \sum_{I=1}^{N\text{ states}} N_I^2(t)\right] \tag{2.29}$$

PES evaluations. In either case (coupled or split-operator with frozen Gaussian propagator)

$$\sum_{I=1}^{N\text{ states}} \sum_{J>I}^{N\text{ states}} N_I(t)N_J(t) \tag{2.30}$$

evaluations of the off-diagonal matrix elements are required at each time step. The number of intrastate matrix elements needed is reduced from $O(N^2)$ to $O(N)$ by using the frozen Gaussian propagator in Eq. (2.28). This more favorable scaling can significantly reduce the computational expense of the AIMS method. However, care should be taken when using the frozen Gaussian propagator because it does not conserve the normalization of the wavefunction. Left unchecked, this would destroy the ability to predict branching ratios. Yet, strict single-surface propagation cannot change the relative fraction of nuclear populations on different electronic states. We therefore renormalize the amplitudes of the nuclear basis functions after the single-surface propagation so that this requirement is obeyed. From a quantum mechanical perspective, this is a crude approximation (recall that the exact single-surface propagator does exchange population between basis functions with the same electronic state label). It is, however, an adequate approximation when an ensemble of classical trajectories can provide an adequate description of the exact, quantum mechanical, dynamics. Although this may seem to be an extreme requirement, the basic underlying assumption of the AIMS method is that classical mechanics provides a good zeroth-order propagator in the absence of specific temporally localized quantum mechanical events. Because the quantum mechanical intrastate interactions between trajectories primarily alter the relative phases between trajectories, it is reasonable to assume that it will be difficult to model phase interference effects (e.g. Stueckelberg oscillations [76,77]) with this

approach. The neglect of these interactions may result in errors in the relative phases and therefore in the amplitudes and positions of the oscillations. More research is needed to determine the range of applicability of this approximation.

The saddle-point and split-operator approximations are compatible. However, we see no compelling reason to use the operator splitting without approximating the single-surface propagator. In what follows we refer to the AIMS method with saddle-point approximation as AIMS-SP and refer to the AIMS method with both saddle-point and split-operator factorization (with an approximate renormalized frozen Gaussian single-surface propagator) as AIMS-SP-SO.

Because the AIMS method associates a unique nuclear wavefunction with each electronic state, one has direct access to dynamical quantities on individual states. This is unlike mean-field based approaches that use only one nuclear wavefunction for all electronic states [59]. One can therefore calculate branching ratios

$$n_I(t) = \sum_{k,k'}^{N_I(t)} C_k^{I^*} \mathbf{S}_{Ikk'} C_{k'}^I \tag{2.31}$$

and coherent expectation values

$$\langle O(t) \rangle_I = \frac{\sum_{k,k'}^{N_I(t)} C_k^{I^*} C_{k'}^I \langle \chi_k^I | \hat{O} | \chi_{k'}^I \rangle}{\sum_{k,k'}^{N_I(t)} C_k^{I^*} \mathbf{S}_{Ikk'} C_{k'}^I} \tag{2.32}$$

where $\hat{O}$ can be any operator (e.g., position or momentum). The coherent analysis of the results is compatible with a coupled propagation of the nuclear basis functions. When the AIMS method is used with *no* approximations beyond the use of a finite basis set, the initial amplitudes are propagated simultaneously and the analysis of the results includes the coherence terms, then the results are guaranteed to converge to the exact quantum mechanical results, given a large enough initial basis set and a robust spawning algorithm. An incoherent analysis of the results

$$\langle O(t) \rangle_I = \frac{\sum_{k}^{N_I(t)} C_k^{I^*} C_k^I \langle \chi_k^I | \hat{O} | \chi_k^I \rangle}{\sum_{k}^{N_I(t)} C_k^{I^*} \mathbf{S}_{Ikk} C_k^I} \tag{2.33}$$

is compatible with the IFG approximation. If the IFG approximation and incoherent analysis are used together with the saddle-point and split-operator frozen Gaussian propagator (i.e., AIMS-SP-SO), and a single electronic state is included in the dynamics, then the method is identical to classical mechanics. Thus, as we have required at the very beginning the AIMS method reduces to quantum mechanics in one limit and to classical mechanics in the other. Heller's

frozen Gaussian approximation is obtained when the IFG approximation is used with AIMS-SP-SO, and the final results are analyzed coherently.

E. Comparison to Other Methods

Recently, several other groups have been working to include nuclear quantum effects in AIMD simulations. Path integral approaches [78–87] are attractive because they exhibit the local behavior that is needed for the quantum chemistry/quantum dynamics interface. However, real-time dynamics with path integrals usually requires many more paths than can be practically computed when the PESs are generated by solving the quantum chemical problem directly. Imaginary-time path integral methods converge much more rapidly and provide equilibrium properties including quantum nuclear effects. The first imaginary-time path integral methods using AIMD techniques have appeared [88,89] and been applied to investigate proton tunneling in water [6,90–93]. The centroid molecular dynamics (CMD) method can follow real-time dynamics with a proper treatment of dispersion and zero point effects. Voth and co-workers [94] have recently presented an AIMD implementation of CMD that seems very promising.

It is also possible to merge semiclassical methods with AIMD—for example, the trajectory surface-hopping (TSH) method of Tully [95,96] for nonadiabatic dynamics and a similarly motivated method for tunneling developed by Makri and Miller [97,98]. There have been a few attempts along these lines. The original Tully–Preston surface-hopping method [95] has been used to investigate photoinduced isomerization in a retinal protonated Schiff base analog [99]. The more recent "fewest-switches" variant of TSH [96] has been used to investigate dynamics around conical intersections in the Na_3F_2 cluster [100]. We have used a surface hopping formulation of tunneling [97,98] in conjunction with hybrid DFT electronic structure methods in order to model the proton transfer tunneling splitting in malonaldehyde, obtaining quantitative agreement with experiment [101].

One can also ask about the relationship of the FMS method, as opposed to AIMS, with other wavepacket and semiclassical nonadiabatic dynamics methods. We first compare FMS to previous methods in cases where there is no spawning, and then proceed to compare with previous methods for nonadiabatic dynamics. We stress that we have always allowed for spawning in our applications of the method, and indeed the whole point of the FMS method is to address problems where localized nuclear quantum mechanical effects are important. Nevertheless, it is useful to place the method in context by asking how it relates to previous methods in the absence of its adaptive basis set character. There have been many attempts to use Gaussian basis functions in wavepacket dynamics, and we cannot mention all of these. Instead, we limit ourselves to those methods that we feel are most closely related to FMS, with apologies to those that are not included. A nice review that covers some of the

earlier methods in more detail, with attention also to nonadiabatic dynamics methods, has appeared in the literature [102].

When spawning is not allowed, the FMS method becomes very similar to Heller's FGA approach [46]. The differences depend on the particular variant of the FMS method that is used. As mentioned above, FMS without spawning and using the IFG and SP approximations with coherent analysis of the final results is exactly the FGA method. If one further analyzes the results incoherently, it becomes exactly classical mechanics. Without the IFG approximation—that is, when all the initial wavepackets are fully coupled—the FMS method becomes a form of variational basis set wavepacket propagation. The use of a variational principle in the context of a Gaussian basis set was first suggested, but not implemented, by Heller [63]. Several implementations appeared later [55,64,103–106], and Metiu and co-workers spent considerable effort trying to interpret the nonclassical propagation of position and momentum parameters which results when the TDVP is applied [55,107,108]. In the FMS method, we intentionally avoid the variational propagation of the width, position, and momentum parameters in order to ensure a well-defined classical limit in the absence of spawning. The methods proposed by Skodje and Truhlar [64] are thus the closest analogs, since most of the other variational approaches have applied the TDVP to all of the basis set parameters.

Recently, there has been much effort [50,109,110] devoted to understanding and improving the Herman–Kluk propagator [70,111], which provides a means for determining the time evolution of the coefficients in the FGA without directly coupling trajectory basis functions. These ideas have been interfaced with the semiclassical initial value representation (IVR) with considerable success [112]. It would be difficult to incorporate these methods directly in the context of AIMS because they require second derivatives of the PES, and the number of trajectories required to obtain stable results often exceeds 10^4 even in one- and two-dimensional problems [50,110,113]. Although it seems that there should be a formal connection between the Herman–Kluk formula for the basis function coefficients (derived with stationary phase approximations) and the expression obtained through application of the TDVP in the limit of an infinite basis set, no attempt to make a rigorous connection has yet been reported.

When spawning is allowed, which is invariably the case in our applications, the closest analog to FMS in the context of Gaussian wavepacket methods are the curve-crossing variants of Metiu's minimum error method (CC-MEM) dynamics [56,114,115]. To the best of our knowledge, these were the first attempts to add basis functions to the basis set during the propagation of Gaussian wavepackets. However, the methods were only explored in one dimension, and therefore the question of where and how to place new basis functions was not very important. In high-dimensional problems, this question becomes critical and the spawning algorithm of FMS has been designed with

such problems in mind. A further difference between CC-MEM and FMS is that CC-MEM, like most other variational Gaussian wavepacket methods, applies the TDVP to all basis set parameters, including position, momentum, and width.

Coalson has recently introduced a wavepacket-path integral method [53,116] for nonadiabatic problems which has similarities to FMS. Time is discretized around the nonadiabatic event, as in FMS; but all possible paths with respect to an electronic surface index are then directly enumerated, and the results of propagation with all possible sets of impulsive hops within the nonadiabatic region are summed coherently in a path integral-like expression. An approximation is introduced to maintain the Gaussian shape of the wavepackets as they propagate through the nonadiabatic region. It remains to be seen whether this method can be implemented successfully in problems with more than two nuclear degrees of freedom or more than one nonadiabatic event.

A number of methods for nonadiabatic dynamics formulated directly in phase space—that is, solving the Liouville equation—have been proposed [117–121]. These also have some similarity to FMS, with the possible advantage of avoiding the averaging over wavepackets that is necessary to model finite temperature effects in a Schrödinger equation-based approach. Kapral and Ciccotti have stressed that it may be more appropriate to mix quantum and classical treatments of different nuclei within the context of the quantum mechanical Liouville equation [120]. Within the FMS approach, the mixed quantum-classical nuclear problem is conceptually sidestepped by treating all degrees of freedom quantum mechanically. In practice, it is not clear whether this avoids the problem when small basis sets are used. These Liouville methods are promising, but, again, it remains to be seen how they will fare in high-dimensional cases with multiple nonadiabatic events.

Perhaps the most popular method for nonadiabatic dynamics has been Tully's "surface-hopping" method (TSH). Of course, the whole idea of spawning has some similarity to the surface hops in TSH. Nevertheless, there are key differences between the methods. The FMS method in all of its variants possesses a well-defined nuclear wavefunction, and therefore it is straightforward to extract correlation functions and spectra, as we have shown in past work [122]. However, even when one restricts the analysis to branching ratios and momentum distributions, there remain differences. We have applied [38] the FMS method directly to the one-dimensional problems first used to test the "fewest-switches" form of TSH [96], and the results point out two possible problems with TSH which can be resolved in FMS. First, phase interference effects in FMS come about through the interaction of different basis functions, that is, trajectories. In the TSH method, these interferences are modeled through phase evolution on different electronic states along a single trajectory. Complete averaging of these interferences would lead to the disappearance of nonadiabatic effects—Prezhdo and Rossky [123] have referred to this as the "quantum

Zeno paradox." On the other hand, recovering these interferences from a single path leads to excessive correlation, as evidenced by the highly oscillatory results obtained with TSH for Tully's third, "extended coupling with reflection," model. This is remedied effortlessly in FMS, and one may speculate that FMS will tend to the opposite behavior: Interferences that are truly present will tend to be damped if insufficient basis functions are available. This is probably preferable to the behavior seen in TSH, where there is a tendency to accentuate phase interferences and it is often unclear whether the interference effects are treated correctly. This last point can be seen in the results of the second, "dual avoided crossing," model, where the TSH results exhibit oscillation, but with the wrong structure at low energies. The correct behavior can be reproduced by the FMS calculations with only ten basis functions [38].

A much more detailed comparison of TSH and FMS-M ("minimal" FMS, employing the IFG and SP approximations and incoherent analysis of final results) has been carried out [124] for a six-dimensional problem where exact results are available. Although the FMS-M method generally improves on TSH results, there are residual errors whose origin remains undetermined. We refer the reader to this paper for a detailed comparison of the TSH and FMS-M methods as applied to a particular problem. Here, we only want to point out the major advantage of the FMS methods over TSH, which is that FMS forms a hierarchy of methods, culminating in the exact solution of the nuclear Schrödinger equation. Even though one may never reach the ideal of converged quantum nuclear dynamics in high-dimensional problems, one can carry out test calculations to assess the effects of improving the calculation. For example, one can increase the size of the initial basis set, decrease spawning thresholds, increase MULTISPAWN, and use alternative methods for evaluating the required integrals—for example, higher-order SP approximations or numerical quadrature. In contrast, it is difficult or impossible to assess the accuracy of the approximations in TSH without recourse to an exact calculation for comparison.

F. Advanced Topics

The previous subsections defined the AIMS method, the various approximations that one could employ, and the resulting different limits: classical mechanics, Heller's frozen Gaussian approximation, and exact quantum mechanics. As emphasized throughout the derivation, the method can be computationally costly, and this is one of the reasons for developing and investigating the accuracy of various approximations. Alternatively, and often in addition, one could try to develop algorithms that reduce the computational cost of the method without compromising its accuracy. In this subsection we discuss two such extensions. Each of these developments has been extensively discussed in a publication, and interested readers should additionally consult the relevant papers (Refs. 125 and 41, respectively). We conclude this subsection with a discussion of the first steps

that we have taken to treat tunneling effects within the framework of the AIMS method [126].

1. *Interpolated Potential Energy Surfaces*

The two primary advantages of *ab initio*-based molecular dynamics methods (flexibility in the PESs and avoidance of tedious fitting to empirical functional forms) come at a challenging computational cost, especially for photochemical problems where electronic excited states and nonadiabatic couplings are required. At the same time, information about the PESs obtained during the propagation is typically discarded, and therefore one does not benefit from the fact that the nuclei may often visit similar regions in configuration space. In particular, the dynamics of certain highly harmonic modes (e.g., C–H stretches) may be quite trivial.

One way to address this issue is to combine first-principles dynamics with automatic interpolation of PESs. For nonadiabatic dynamics, interpolation alone is problematic because the adiabatic PESs often have sharp features near the region of strong interstate coupling. Any smooth interpolating function will fail to reproduce these sharp features in the PESs as well as the often strongly varying nonadiabatic coupling. While both difficulties can be avoided by using a diabatic representation of the electronic states, we insist on using the adiabatic representation in the AIMS method for two reasons. First, the diabatic representation is not unique and, without information about the electronic wavefunction at different geometries, is often path-dependent. Second, for chemical applications the nuclear kinetic energy is typically low (i.e., thermal), making the adiabatic representation more natural. In practice, this means that fewer basis functions will need to be spawned. By using *ab initio* methods for configurations near conical intersections while interpolating the PESs (and not their couplings) elsewhere, we can overcome the nonsmoothness problems.

We have chosen to use the modified Shepard interpolation scheme introduced by Collins and co-workers [127–131]. At any nuclear configuration $\mathbf{R}$, the potential energy, $V(\mathbf{R})$, is represented as a sum of Taylor expansions in reciprocal bond lengths, $\mathbf{Z}$. Each of these Taylor expansions is centered at a different data point, $Z(i)$, and is truncated at second order, although higher derivatives may in principle be included if desired. The choice of internal coordinates minimizes the number of data points required for the interpolation. As Collins and co-workers have shown [132], the correct identical particle symmetry may be enforced on the PESs by extending the data set to include all possible permutations of each data point. For simplicity we ignore this symmetry issue and hence write the interpolated potential energy as

$$V(\mathbf{R}) = \sum_i w_i(\mathbf{Z}) T_i(\mathbf{Z}) \tag{2.34}$$

where w_i is a normalized weight function which ensures that the patching of the Taylor polynomials, T_i, is smooth:

$$w_i(\mathbf{Z}) = \frac{|\mathbf{Z} - \mathbf{Z}(i)|^{-p}}{\sum_j |\mathbf{Z} - \mathbf{Z}(j)|^{-p}} \tag{2.35}$$

where p must be taken [128] such that $p > (3N - 6) + q$, where q is the order of the Taylor expansion. This purely geometric requirement ensures that the weight function decreases faster than the increase of the Taylor expansion. The way in which one chooses where in configuration space to place the data points is crucial, and Collins et al. [127–130] have developed an iterative algorithm for choosing these points. Briefly, new data points are selected from configurations visited by n_t classical trajectories calculated on the PES interpolated from the data set of the previous iteration. The process begins by calculating a few tens of data points along some minimum energy path from reactants to products, and it is deemed converged when an observable of interest ceases to change with the addition of more data.

Not all the data points from the n_t trajectories are used in the interpolation. The n_{sel} new data points are selected using the "h weight" function [133] that balances the desire to place new points as far as possible from the existing n_d data points with the need to have a higher data density in dynamically important regions. In particular, the relative importance of a candidate data point $\mathbf{Z}^k$ (k denotes the trajectory) is given by

$$h[\mathbf{Z}^k] = \frac{\sum_{j \neq k}^{n_d} |\mathbf{Z}^k - \mathbf{Z}^j|^{-p}}{\sum_{i=1}^{n_d} |\mathbf{Z}^k - \mathbf{Z}(i)|^{-p}} \tag{2.36}$$

This criterion is based on pure geometric considerations. When the second derivatives must be computed by finite differences of analytic gradients, as is often the case in practice for highly correlated electronic wavefunctions, it can be improved by a "prescreening" procedure. Before calculating the energy and gradients at small (positive and negative) displacements of a proposed new data point, $\mathbf{R}_{\text{new}}$, the values of the interpolated and *ab initio* potential energies are compared. If they agree within the target accuracy of the PES, the point is not added to the data set and the second derivative matrix is not evaluated. This results in considerable computational savings, with little or no loss of accuracy, because many calculations are required to obtain the second derivative information whereas only one is required for the energy.

The interpolation method was extended to include multiple electronic states by requiring that the same data points be used to interpolate all electronic states. These points were chosen (by the prescreened h-weight procedure) from classical trajectories that run alternately on each of the electronic states.

Because the concept of minimum energy path is not well-defined when multiple electronic states are involved, the initial data set is simply taken as the union of points which one considers important on each of the electronic states—for example, local minima on each electronic state. The weights of each data point, w_i in Eq. (2.34), were taken to be the same on all electronic states because they only depend on the location of the data points. Hence, the difference between electronic states ($V^I_{\text{Shepard}}(\mathbf{R})$) is manifested only in the parameters of each of the Taylor expansions:

$$V^I_{\text{Shepard}}(\mathbf{R}) = \sum_i w_i(\mathbf{Z}) T^I_i(\mathbf{Z}) \tag{2.37}$$

Because the Shepard interpolation method is global, it is affected by cusped regions in the PES. To avoid this we must define a crossing or nonadiabatic region where the Shepard interpolation will likely fail. Because we do not interpolate the nonadiabatic coupling, we define this region using a threshold energy gap (and not a threshold effective nonadiabatic coupling), ΔE_{min}. Attempts to fit cusped regions are then avoided by rejecting all data points for which the energy gap (between any pair of electronic states) is less than ΔE_{min}. In these surface-crossing regions, the interpolation function is replaced by direct *ab initio* evaluation of the PESs (and their couplings). As with the spawning threshold previously discussed, the precise value of this parameter is somewhat arbitrary. If it is too small, the interpolation will converge slowly when conical intersections are present. If it is too large, large regions of the PES will be modeled by direct *ab initio* evaluation, making the procedure more costly than necessary.

The *ab initio* and interpolated potential functions are coupled using a smooth switching function, written in terms of the energy difference between the electronic states:

$$V^I(\mathbf{R}) = w(\mathbf{R}) V^I_{ab\ initio}(\mathbf{R}) + (1 - w(\mathbf{R})) V^I_{\text{Shepard}}(\mathbf{R}) \tag{2.38}$$

where

$$\tilde{w}(\mathbf{R}) = \frac{1}{2}\left[1 + \tanh\left(\frac{\Delta E(\mathbf{R}) - \Delta E_c}{\Delta E_w}\right)\right] \tag{2.39}$$

and

$$w(\mathbf{R}) = \begin{cases} 0, & \tilde{w}(\mathbf{R}) < w_{\text{threshold}} \\ 1, & \tilde{w}(\mathbf{R}) > 1 - w_{\text{threshold}} \\ \tilde{w}(\mathbf{R}), & \text{otherwise} \end{cases} \tag{2.40}$$

In Eq. (2.39), $\Delta E(\mathbf{R})$ is the minimum (over all pairs of electronic states considered) of the absolute value of the energy gap at the given nuclear geometry, $w_{\text{threshold}}$ is a numerical parameter taken small enough ($\approx 10^{-5}$) that it has no effect on the dynamics, and ΔE_c and ΔE_w are the center and range of the switching function, respectively.

This hybrid approach can significantly extend the domain of applicability of the AIMS method. The use of interpolation significantly reduces the computational effort associated with the dynamics over most of the timescale of interest, while regions where the PESs are difficult to interpolate are treated by direct solution of the electronic Schrödinger equation during the dynamics. The applicability and accuracy of the method was tested using a triatomic model: collisional quenching of Li(p) by H_2 [125], which is discussed in Section III.A below.

2. *Time-Displaced Basis Set*

We have investigated another procedure for reducing the computational expense of the AIMS method, which capitalizes on the temporal nonlocality of the Schrödinger equation and the deterministic aspect of the AIMS method. Recall that apart from the Monte Carlo procedure that we employ for selecting initial conditions, the prescription for basis set propagation and expansion is deterministic. We emphasize the deterministic aspect because the time-displaced procedure relies on this property.

The time-displaced basis (TDB) method incorporates information about the PES in the region spanned by the wavefunction at previous times without resorting to interpolation. It can significantly reduce the number of matrix element evaluations (normally scaling quadratically with the number of basis functions) without compromising the quality of the results. As we will show, under certain assumptions it is possible to reduce the scaling of the procedure from quadratic to linear in the number of basis functions. The basic idea is as follows: Instead of choosing N_{init} independent initial basis functions (using a MC procedure), choose only N_s independent initial basis functions, where $N_s < N_{\text{init}}$. The basis set is then enlarged to N_{init} by adding $N_{\text{init}} - N_s$ basis functions that are displaced forward and backward in time with respect to the N_s independent basis functions. This is motivated by the observation that one can cover a given energy shell in phase space either by generating many independent trajectories or by following a single trajectory for a long time. This is not meant to imply that one will be able to achieve anything approaching complete coverage of the accessible phase space for multi-dimensional problems. Rather, we point out that there are two independent ways of expanding the basis set: multiple independent classical trajectories and time displacement along these trajectories. To better understand this idea, consider the simple example of $N_{\text{init}} = 3$ and $N_s = 1$. Instead of choosing three independent basis functions, we choose only one and refer to it as the "seed." (The position and momentum that

define a seed basis function are chosen randomly from the appropriate Wigner distribution at $t = 0$.) Two additional TD basis functions are associated with the seed and are related to it by forward and backward propagation in time. Because classical mechanics guides the propagation of the nuclear basis functions, a single distinct path is traveled by the three basis functions. This path is defined by the basis function that at $t = 0$ is most forward displaced in time, and all other basis functions belonging to the same seed follow this path. Because the spawning procedure is deterministic, this property carries over to the next generation of basis functions: The ones spawned by the "head" basis function define the path that is traversed by all the other spawned basis functions that are children of basis functions belonging to the same seed.

To quantify the resulting reduction in computational cost, we compare the number of matrix element evaluations for N_{init} independent basis functions to that required when only N_s of these N_{init} are independent. The total number of basis functions is N_{init} in both cases. For simplicity, we ignore the symmetry of the Hamiltonian matrix—we assume that all N_{init}^2 elements are evaluated even though $\mathbf{H}$ is Hermitian. When all N_{init} basis functions are independent, traveling on N_{init} distinct paths in phase space, N_{init}^2 matrix element evaluations are required at each time step. When the total number of basis functions is N_{init}, but only N_s distinct paths are traversed by these N_{init} basis functions, the number of matrix element evaluations reduces to $O(N_s^2 + N_s N_{\text{init}})$. The number of matrix elements is no longer quadratic in N_{init}, but rather linear. This result is illustrated in Fig. 5. Here, the total number of basis functions is six, and there are two seeds (i.e., $N_s = 2$). For clarity the two seeds are spatially separated (in reality, basis functions that belong to different seeds are not so neatly separated), and within each seed the "leading" (in time) basis function is shaded. The basis set is shown at two time points, t and $t + \Delta t$. At each point in time, any matrix element that involves a shaded basis function must be evaluated, and these are denoted by arrows connecting basis functions. This is to be compared with the case where all basis functions are independent. In this specific example, 11 matrix elements are required for the TDB set while 21 are required if all basis functions are chosen independently.

The key question is how many independent initial conditions are required for a basis set of size N_{init}. While one would like to minimize the number of seeds, the quality of the results is bound to deteriorate if too few are used. There is no general answer to this question, and therefore this number should be viewed as another parameter that defines the basis set and governs the numerical convergence of the method. For each class of problems, numerical tests should be used to determine N_s. Our experience with this procedure is limited, and therefore we make only one general comment. The number of independent initial conditions must be large enough so that its energy spectrum faithfully mimics the energy spectrum of the initial wavefunction $\Psi_{t=0}^{\text{exact}}$. As a

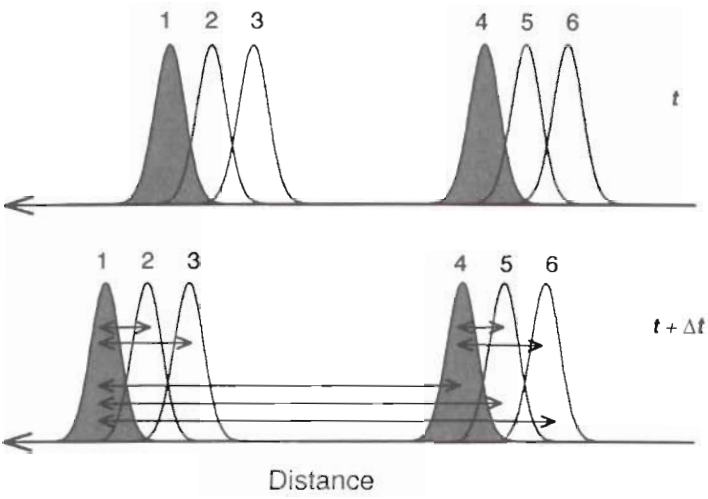

Figure 5. Schematic illustration of the time evolution of a time-displaced basis. Basis states 1, 2, and 3 belong to one seed while 4, 5, and 6 belong to another. The basis set is shown at two time points, and the leading basis functions are shaded in gray. The arrows connecting basis functions indicate required new matrix elements at time $t + \Delta t$. For this specific example, 11 new matrix elements are evaluated at each point in time, compared to 21 if all basis functions had been chosen independently. (Figure adapted from Ref. 40.)

consequence of the uncertainty principle, the quantum mechanical "phase space" accessed by the wavefunction is not restricted to lie on a classical energy shell, but rather will have a finite energy width which can never be modeled with a single classical trajectory, time displaced or not. Therefore, the limit of a single seed should not be expected to be sufficient.

The TDB approach can be applied alone or combined with the hybrid approach discussed in the previous section. We have tested it using a two-dimensional analytical model, and some of the results are presented in Section III.A. A more extensive discussion can be found in Ref. 41.

3. *Tunneling*

So far our discussion of the AIMS method has only emphasized quantum effects that are due to breakdown of the Born–Oppenheimer approximation. There are other instances when classical mechanics fails to describe the dynamics, and in this subsection we discuss an extension of the AIMS method that incorporates tunneling effects. Unlike the previous two subsections, this extension does not attempt to reduce the computational cost of the method but rather to expand its scope. This extension to the AIMS method affects only the spawning algorithm.

All other aspects of the method (e.g., selection of initial conditions, propagation, and analysis of the results) remain the same.

Because the development of the AIMS method relied on the concept of nonadiabatic regions, significant modifications/additions are needed if tunneling effects are to be modeled. In the original prescription, the basis set was allowed to expand only during nonadiabatic events and only between different electronic states. Within this framework, tunneling effects can occur only if they are mediated by a second electronic state—that is, when they accompany an electronically nonadiabatic event. Under thermal conditions the Born–Oppenheimer approximation works well and therefore one would like to incorporate tunneling effects even when the dynamics is electronically adiabatic. Because tunneling is intrinsically nonclassical, some form of spawning procedure will be required—this time on the same electronic state. To determine where and when spawning is required, an analog to the concept of "nonadiabatic event" will be introduced. As for the multielectronic state case, the development of the algorithm was dictated by the requirement of compatibility with quantum chemistry. In particular we have assumed that information about the PES is limited and local; that is, the PES is known only at a few geometries and is generated "on the fly."

The algorithm that we have developed requires labeling of N_T tunneling particles and N_{DA} donor/acceptor particles. The former includes all the particles that will be allowed to tunnel during the simulation (e.g., protons), and the latter describes all the particles that can be covalently attached to a tunneling particle. The distinction between a donor and acceptor simply denotes whether or not the particle is currently covalently attached to a tunneling particle, and a distance-based criterion is used to determine this. During the simulation, donor and acceptor particles can change their identity, but both they and the tunneling particles have to be identified at the beginning of the calculation. The balance between basis set size and accuracy is kept by two numerical parameters, namely, the tunneling threshold (R_T) and the number of basis functions that will be spawned per tunneling event (MULTISPAWN). The tunneling threshold is analogous to the spawning threshold, λ_0, and it defines the minimum extension of a covalent bond involving a tunneling particle that suffices to indicate that a tunneling event should be considered. The magnitude of R_T controls the propensity to add new basis functions (the smaller the value of R_T, the greater the number of basis functions that are likely to be added). As in the multielectronic state case, higher accuracy is achieved by increasing MULTISPAWN and decreasing R_T.

At each time step, and for a tunneling particle within each nuclear basis function, we check whether a tunneling event might be occurring. We first determine its current donor particle, defined as the current donor/acceptor particle to which it is closest. If this distance is shorter than R_T, this particle

does not need to be considered further, until the next time step. On the other hand, if this distance exceeds R_T, the particle should be allowed to tunnel. In such a case we displace the tunneling particle along the tunneling vector(s), R^i_{Tunnel}. There are $N_{DA} - 1$ tunneling vectors per tunneling particle. To determine them, we place the tunneling particle next to each acceptor and quench the system to its local minimum. From the resulting $N_{DA} - 1$ local minima, only those with potential energy less than the current total energy are considered further. R^i_{Tunnel} is defined as the vector connecting (a) the local minimum where the tunneling particle is bound to its current donor to (b) the one where it is bound to the ith acceptor. For each local minimum that remains under consideration, we propagate the basis function until a classical turning point along the tunneling vector is reached (at time t_{tp}) or until the tunneling particle is closer to the new minimum than the old one. In the latter case, the acceptor can be reached classically, and therefore there is no need to consider this path/tunneling event. If a turning point was reached, we displace the basis function along R^i_{Tunnel} until a new classically allowed region is encountered and record the position and momentum of all the particles at that point. The basis function is then back-propagated for time $t_{bp} = t_{tp} - t_0$, where t_0 labels the beginning of the tunneling event. This brings the parent basis function back to the point where its uncoupled (classical) propagation began. Within the back-propagation time, t_{bp}, MULTISPAWN new basis functions are spawned with zero population. The initial conditions for the MULTISPAWN new basis functions are obtained by back-propagation of a trajectory using the positions and momenta recorded when the new classically allowed region was reached. This procedure is repeated for all tunneling particles and for all basis functions. When it is completed, the coupled propagation of the basis functions and their coefficients proceeds. A flow chart of the algorithm is provided in Fig. 6.

Whereas the multi- and single-surface spawning algorithms are different (the former allows only for spawning on a different electronic state, and the latter allows only for spawning on the same electronic state), the physical motivation for both is the same: We first attempt to identify and discretize the quantum mechanical events and then determine the initial conditions for the newly spawned basis functions. The spawning events are isolated by identifying the physical property that triggers basis set expansion: nonadiabatic coupling in the multistate problem and distance in the single state (tunneling) problem. Initial conditions are obtained by propagating the parent basis function through the tunneling or nonadiabatic region. This propagation is straightforward in the multistate case, but it poses a problem in the tunneling case because the selection of the direction of the tunneling path (that determines the position of the new basis functions) is not obvious. The optimal choice of this path has been discussed in many papers [134–137]. We have proposed to use a simple, straight-line path (in the full multidimensional coordinate space). We believe

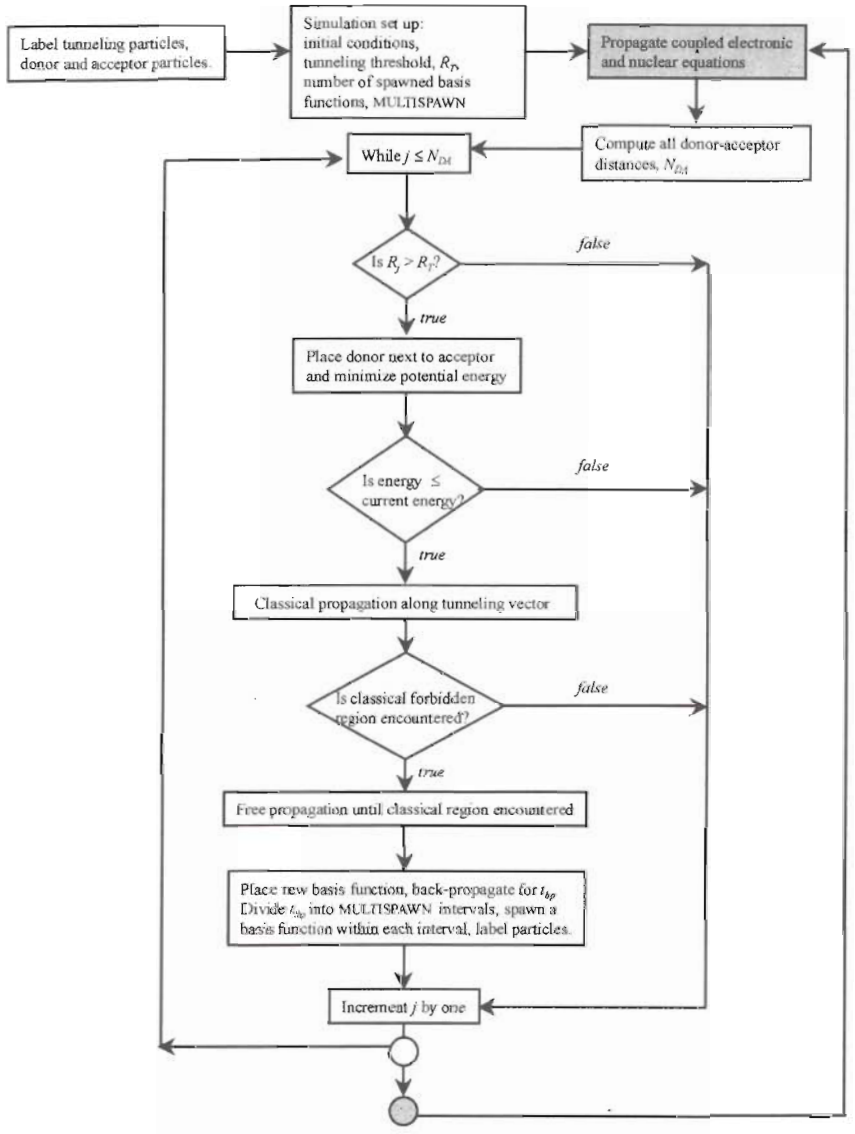

Figure 6. Flow chart of the multiple-spawning code and the spawning algorithm for the case of single-state spawning. The spawning algorithm is executed after each propagation time step (upper-rightmost rectangle). When the execution of the algorithm is completed, the program returns to the propagator (gray circle at bottom of sketch.) For clarity, only a single tunneling particle is considered in this sketch. (Figure adapted from Ref. 126.)

that in the absence of detailed global information about the PES, this is the only viable choice.

This algorithm attempts to be general and is therefore rather complicated—certainly more complicated than the multisurface spawning algorithm. Our experience with it is limited to two-dimensional model problems [126], and therefore we cannot be certain about its generality. Because it requires a preassignment of tunneling particles and donors and acceptors and also because the choice of the tunneling vector is not obvious, it will be harder to demonstrate stability of the final results than it has been for the multisurface algorithm. The results will depend on the placement of new basis functions, and careful investigations will be required in order to optimize the placement of new basis functions and test the validity of the procedure.

III. APPLICATIONS AND NUMERICAL CONVERGENCE

In this section we discuss the accuracy of the AIMS method and review some applications. Considerably larger molecules can be studied with the FMS method if one is willing to use empirical functional forms; for example, we have carried out calculations of photochemistry in retinal protonated Schiff base [138] and bacteriorhodopsin [139]. The nuclear wavefunction in the latter calculation includes more than 11,000 degrees of freedom. In the following, we restrict our discussion to AIMS applications that solve the electronic Schrödinger equation simultaneously with the nuclear dynamics. However, when discussing numerical convergence, we will alternate between AIMS and FMS depending on whether it is convergence of the electronic structure or nuclear dynamics which is being discussed.

A. Applications

We review three systems to which the AIMS method has been applied. The first is the collision-induced electronic quenching of Li($2p$) by an H_2 molecule [140]. This is perhaps the simplest realistic example of electronic to vibrational/translational energy transfer and can therefore serve as a useful paradigm for understanding electronic quenching. The electronic states relevant to the collision-induced quenching process can be labeled as Li($2s$)$+H_2$ and Li($2p$)$+H_2$, where the p orbital in the second state is aligned parallel to the H_2 molecular axis. An OA-HF-CAS(2,2)*S electronic wavefunction (and a double-ζ quality basis set [141,142]) was used in the calculations and the initial state of the system is nonstationary. The Li atom is far (8 Å) from the center of mass of the H_2 molecule that is in a coherent rotational–vibrational state chosen according to the quasi-classical prescription to model $v = 0, j = 0$. At this level of theory, the system exhibits a conical intersection at an atom–diatom distance of 2.86 bohr. The form of the potential energy surfaces in the vicinity of the

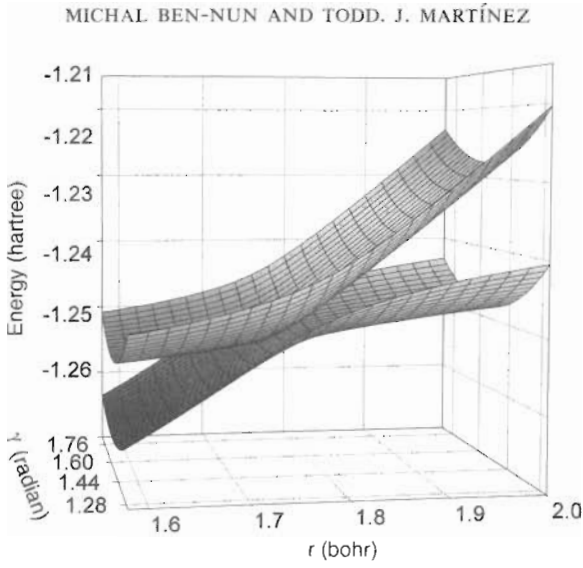

Figure 7. Two-dimensional cut of the ground- and excited-state adiabatic potential energy surfaces of $Li + H_2$ in the vicinity of the conical intersection. The $Li–H_2$ distance is fixed at 2.8 bohr, and the ground and excited states correspond to $Li(2s) + H_2$ and $Li(2p) + H_2$, where the p orbital in the latter is aligned parallel to the H_2 molecular axis. γ is the angle between the H–H internuclear distance, r, and the Li-to-H_2 center-of-mass distance. Note the sloped nature of the intersection as a function of the H–H distance, r, which occurs because the intersection is located on the repulsive wall. (Figure adapted from Ref. 140.)

conical intersection is shown in Fig. 7, where the $Li–H_2$ distance is fixed to $R = 2.86$ bohr and γ is the angle between R and the H_2 internuclear distance, r. Accessing the conical intersection requires stretching of the H_2 bond beyond the usual outer classical turning point at the zero point energy. Because the intersection is located on the repulsive walls of the PESs, it is strikingly sloped, deviating quite strongly from the model conical form that is often discussed. Of course, in a small enough neighborhood around the intersection a conical form is guaranteed, although it may be tilted [143,144].

Commonly, it is asserted that upward transitions from the lower adiabat to the upper one should be less likely than downward transitions because of the "funneling" property of the intersection [144,145]. This is clearly seen in the usual model conical intersection—as seen, for example, in Fig. 1 of Ref. 146, where there is (a) a well, or "funnel," in the upper adiabat which guides the wavepacket to the intersection and (b) a peak on the lower adiabat which tends to guide the wavepacket away from the intersection. The potential energy surfaces shown in Fig. 7 differ from this canonical picture, and in particular it is not at all clear that the wavepacket on the lower adiabatic state will be funneled away from the intersection. For the conditions chosen in our calculations, we

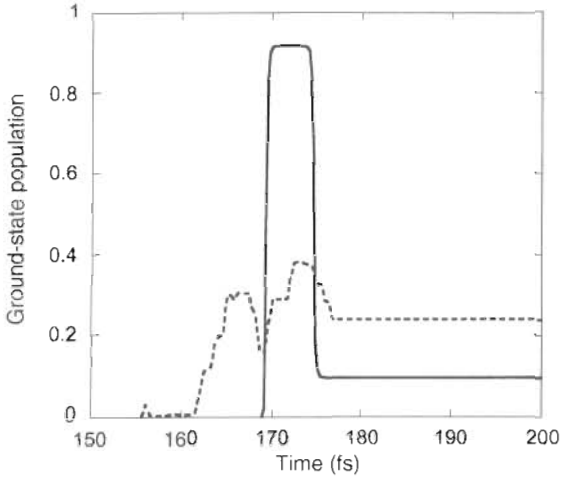

Figure 8. $Li+H_2$: Ground-state population as a function of time for a representative initial basis function (solid line) and the average over 25 (different) initial basis functions sampled (using a quasi-classical Monte Carlo procedure) from the $Li(2p)+H_2(v=0,\ j=0)$ initial state at an impact parameter of 2 bohr. Individual nonadiabatic events for each basis function are completed in less than a femtosecond (solid line); and due to the sloped nature of the conical intersection (see Fig. 7), there is considerable "up-funneling" (i.e., back-transfer) of population from the ground to the excited electronic state. (Figure adapted from Ref. 140.)

found that the nuclear population on the lower adiabatic state is not funneled away from the intersection sufficiently quickly. Consequently, there is efficient recrossing (back to the upper adiabatic state) and therefore inefficient quenching. This "up-funneling" phenomenon is demonstrated in Fig. 8, which shows the ground-state population as a function of time for a particular (arbitrarily chosen) set of initial conditions (solid line). As expected for quenching of a localized wavepacket via a conical intersection, the population transfer is extremely fast (individual nonadiabatic events are completed in less than a femtosecond). More interestingly, the ground state is populated and then immediately depopulated. The first transition corresponds to a downward transition from the upper to the lower adiabatic electronic state and is fully expected. The second transition, however, is an upward transition. This behavior is in contrast to the common view that conical intersections should serve as "funnels" directing population toward the lower adiabatic state. Because the conical nature of an intersection is operative over some lengthscale, which (depending on the nuclear velocity) may or may not be relevant to the nuclear dynamics, the assertion that downward transitions dominate at a conical intersection can be called into question. For the $Li+H_2$ system (and our particular choice of initial conditions) this assertion is incorrect, and in general

the veracity of such statements will depend on the topography of the conical intersection and the nuclear velocities. A recent study by Yarkony [147] investigates funneling and up-funneling behavior in a two-dimensional model conical intersection, supporting these conclusions.

One expects the timescale of the nonadiabatic transition to broaden for a stationary initial state, where the nuclear wavepacket will be less localized. To mimic the case of a stationary initial state, we have averaged the results of 25 nonstationary initial conditions and the resulting ground-state population is shown as the dashed line in Fig. 8. The expected broadening is seen, but the nonadiabatic events are still close to the impulsive limit. Additional averaging of the results would further smooth the dashed line.

The $Li+H_2$ problem was used to test the *ab initio*/interpolated extension of the AIMS method. As described in Section II.F [125], the interpolation function is called on to represent the smooth regions of the potential energy surfaces, while *ab initio* quantum chemistry, in this case full configuration interaction, represents the regions near conical intersections and the nonadiabatic coupling between electronic states. The accuracy of the hybrid approach was investigated by (1) comparing various cuts of the potential energy surfaces, (2) comparing time traces of individual trajectories/basis functions, and (3) comparing averaged expectation values. In Fig. 9 the hybrid and fully *ab initio* excited-state potential energy surfaces are compared (the system is constrained to C_{2v} symmetry). Explicit comparison of the *ab initio* and hybrid interpolated/*ab initio* surfaces shows RMS errors of 0.63 and 0.69 kcal/mol on the ground- and excited-state potential energy surfaces, respectively. The ground- and excited-state PESs vary by 3.0 and 1.5 eV over this region. The final (averaged) branching ratios were also in good agreement: 51% quenching for the hybrid method and 54% for the full *ab initio* dynamics. (For a comparison of individual time traces as well as averaged ones see the original paper, Ref. 125.) The computational effort associated with the hybrid method was over an order of magnitude less than that for the full *ab initio* dynamics, an impressive reduction given the high accuracy of the interpolated surfaces. The results are encouraging, but it remains to be seen whether similar accuracy and reduction in computational effort can be obtained for larger systems (10–20 atoms).

A second molecule that we have studied using the AIMS method is ethylene. The photochemistry of ethylene is interesting as a paradigm for *cis–trans* isomerization in unsaturated hydrocarbons. Unsaturated alkanes pose a challenge to quantum chemistry because the description of their lowest excited electronic states requires careful treatment of electron correlation. For example, the ordering of the lowest-lying singly and doubly excited electronic states (B_u and A_g, respectively) is sensitive to the details of the wavefunction used. In the case of butadiene, this ordering has been the topic of a long controversy [148].

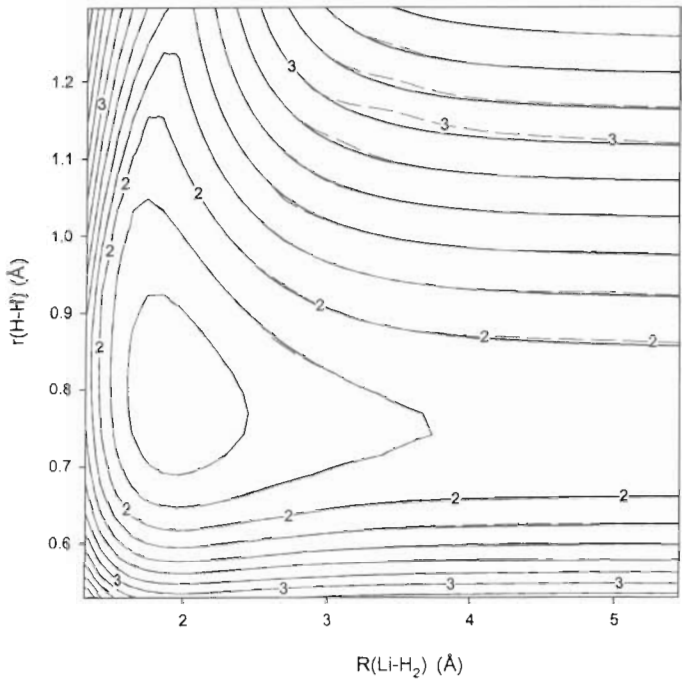

Figure 9. Comparison of *ab initio* (full line) and *ab initio*/interpolated (dashed line) potential energy surfaces for the first electronically excited state of $Li + H_2$ system restricted to C_{2v} geometry. Contours are labeled in eV. (Figure adapted from Ref. 125.)

Because ethylene is the shortest unsaturated hydrocarbon, its photochemistry is special in some respects. Simple particle-in-a-box considerations suggest (and theory and experiment confirm) that ethylene will have the largest excitation energy (as compared to longer conjugated systems). At the same time, ethylene also has a small number of internal modes. Consequently, photoexcitation of ethylene leads to fragmentation in addition to the isomerization that is the hallmark of longer polyenes [149–151]. This added complexity is in addition to some unresolved issues regarding the absorption and resonance Raman spectrum of ethylene, which are partially due to our incomplete knowledge of the character of the manifold of excited electronic states. Nevertheless, certain crude statements about the singly excited state of ethylene can be made. Upon absorption of a photon, an electron is promoted from a bonding π molecular orbital (*MO*) to an antibonding π^* *MO*. The ground electronic state of ethylene is planar and stable with respect to twisting, whereas the $\pi\pi^*$ state favors a twisted D_{2d} geometry that minimizes both the kinetic energy associated with the antibonding π^* orbital and the Coulomb repulsion between the p electrons of the

two carbon atoms. Consequently, the electronic excitation results in geometric relaxation toward a stretched (formally the bond order is reduced from two to one) and twisted geometry. The conventional picture of photoisomerization indeed identifies torsion about the C=C bond as the reaction coordinate and concentrates on the $\pi\pi$ and $\pi\pi^*$ electronic states. Computation of the ground and singly excited potential energy surfaces along this coordinate shows that this view is considerably oversimplified (regardless of the detailed way in which the bond and angle coordinates are allowed to vary). In particular, the minimal S_0–S_1 energy gap that results is approximately 60 kcal/mol, implying a long excited-state lifetime and significant fluorescence. Yet there is no detectable fluorescence from the excited state of ethylene. The absence of fluorescence suggests a short excited-state lifetime, which has recently been investigated using femtosecond pump-probe spectroscopy [152].

The broad and diffuse absorption spectrum of ethylene has been assigned by Wilkinson and Mulliken [153] to the $\pi \rightarrow \pi^*$ valence (V) and Rydberg (R) states. Based on an isoelectronic analogy between O_2 and C_2H_4, they assigned the single progression in the V state band to the C=C stretching motion [153]. Later investigators questioned this assignment and suggested a purely torsional progression [154]. Next, based on a spectral study of ethylene isotopomers, Foo and Innes [155] agreed with the reassignment but suggested a mixture of stretching and torsion. When theoretical investigation [156] predicted that the change in the C=C bond length on the V state was less than 0.1 Å, Mulliken himself became convinced that the torsion dominated the spectrum [157,158]. The accepted assignment of mixed torsion and stretching was challenged by Siebrand and co-workers [159] who presented theoretical evidence that there is no visible stretching activity in the spectrum. Consequently, there have been few challenges to the torsional assignment of the spectrum, but recently the very identity of the bands has been questioned [160]. These uncertainties regarding the excited-state motion were exacerbated when the possible role of the pyramidalization coordinate was suggested.

The pyramidalization coordinate of ethylene (and longer polyenes) has been first studied in the context of the concept of "sudden polarization." Salem and co-workers [161–163] noted that mono-pyramidalization of ethylene (keeping the molecule in C_s symmetry) results in a large dipole moment. The onset of this phenomenon is quite sudden; that is, small distortions result in a large change in the dipole moment (which is zero by symmetry at both the planar and twisted geometries). This arises due to an avoided crossing between the valence and ionic states (V and Z in Mulliken's notation) near the twisted (nonpyramidalized) geometry. The original speculation that the electrical signal thus generated might trigger conformational changes in the visual pigment proteins [162] was abandoned when it was shown that proton transfer was required for vision [164]. Irrespective of its importance in the retinal protonated Schiff base

chromophore of visual pigments, and in spite of the crude electronic structure treatment that led to the original observation, both experiment and theory suggest that the pyramidalization coordinate does participate in the excited-state dynamics. The theoretical evidence is based on restricted excited-state optimizations that found mono-pyramidalization to be a stabilizing distortion [165,166]. Resonance Raman experiments find overtone activity in both out-of-plane wagging and rocking vibrations [167], supporting a role for pyramidalization in the initial motion of ethylene following the electronic excitation.

Using a GVB-OA-CAS(2/2)*S wavefunction and a double-ζ quality basis set, we have carried out AIMS simulations of the photodynamics upon $\pi \rightarrow \pi^*$ excitation. In the following we limit our discussion to the photochemical mechanism of *cis–trans* isomerization and fragmentation dynamics, but we have also used AIMS to compute the electronic absorption and resonance Raman spectra [122]. The AIMS simulations treat the excitation as being instantaneous and centered at the absorption maximum. Hence, the initial state nuclear basis functions are sampled from the ground-state Wigner distribution in the harmonic approximation. Ten basis functions are used to describe the initial state and we employ the IFG, SP, and split-operator approximations, that is, AIMS-SP-SO. Overall approximately 100 basis functions are spawned during the dynamics, and we follow the dynamics up to 0.5 ps (using a time step of 0.25 fs).

The first dynamical question to ask concerns the excited-state lifetime. In Fig. 10, we show the AIMS results for the excited-state lifetime as a function of time following photoexcitation at $t = 0$. Both the raw data (solid line) and a Gaussian fit (dashed line) are shown. The inferred time constant of 180 fs is in agreement with the expected subpicosecond dynamics. The decay is clearly nonexponential and its onset is delayed: Appreciable decay from the excited state does not begin until approximately 50 fs after the excitation. The results shown in Fig. 10 have been directly compared to recent pump-probe experiments of Radloff and co-workers [152], where the probe pulse induces ionization of the excited state. Assuming exponential decay of the ionizable excited state, Radloff and co-workers obtained a lifetime of 30 ± 15 fs. If the AIMS simulations are correct, this is much too short to be considered as an excited-state lifetime and the possibility of a dark form of the excited state must be considered. Using the AIMS data and assuming that the molecule ionizes with 100% efficiency provided that the ionization potential is lower than the threshold given by the probe pulse, we have simulated the experiment of Radloff et al. The results are shown in Fig. 11 along with an exponential fit. The excited-state lifetime extracted from this fit (35 ± 2 fs) agrees well with the experimental [152] one (30 ± 15 fs). This agreement is encouraging and important, but it also suggests that the experiment is probing the excited state only within a limited window around the Franck–Condon region, thus providing a lower bound on the excited-state lifetime. In this scenario, most of the

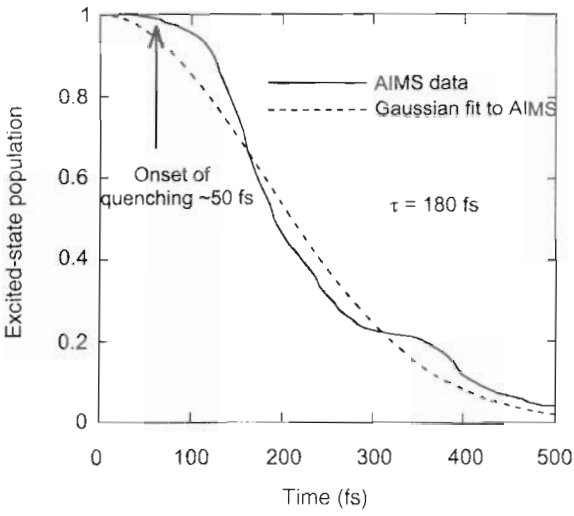

Figure 10. Excited-state population of ethylene as a function of time in femtoseconds (full line). (Results are averaged over 10 initial basis functions selected from the Wigner distribution for the ground state in the harmonic approximation.) Quenching to the ground electronic state begins approximately 50 fs after the electronic excitation, and a Gaussian fit to the AIMS data (dashed line) predicts an excited-state lifetime of 180 fs. (Figure adapted from Ref. 214.)

excited-state dynamics, after significant twisting, which is discussed below, is invisible to the experiment. Furthermore, the AIMS results are clearly poorly modeled by an exponential decay, questioning the wisdom of exponential fitting of the experimental data.

By following the centroids of the dominant nuclear basis functions along with their electronic wavefunction, detailed information about the excited-state (nuclear and electronic) dynamics can be extracted. Following excitation of the planar molecule, the C=C bond stretches and then the molecule begins to twist. After ~50 fs the molecule is typically twisted, but excited-state quenching does not even begin until 50 fs. Therefore torsion is not the sole coordinate responsible for the return to the ground electronic state. Significant quenching to the ground electronic state requires pyramidalization of one of the methylene units. Attempts at hydrogen migration are also observed, but only rarely have we seen the molecule decay to the ground electronic state via a hydrogen-migration conical intersection. The corresponding electronic dynamics involves three electronic states: N, V, and Z in Mulliken notation. The excited-state dynamics can be characterized as consisting of electron transfer between the two methylene units. The intramolecular electron transfer dynamics is punctuated by quenching back to the ground electronic state each time that the excited-state molecule reaches one of the excited-state minima, since these

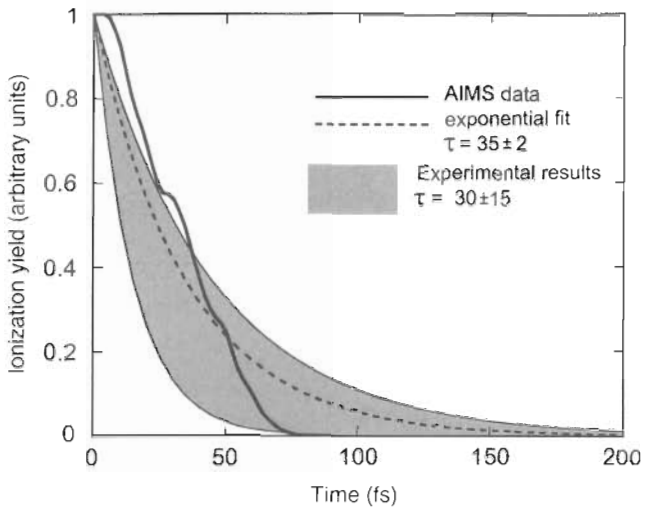

Figure 11. C_2H_3 ion yield as a function of time in femtoseconds for a pump-photoionization probe experiment. Heavy line: Predicted ion yield using the AIMS data and assuming an ionization threshold of 3.5eV. Dashed line: Exponential fit to the AIMS ion yield predicting an excited state lifetime of 35 fs. Gray shaded area: Reported ion yield [152] obtained using an exponential fit to the experimental data predicting an excited state lifetime of 30 ± 15 fs. (Figure adapted from Ref. 214.)

are in close proximity to a conical intersection. This picture of the ethylene photochemistry that involves pyramidalization and torsional motions, and both the V and Z states, is quite different from the conventional one centering on the torsional coordinate and the role of the V state.

One of the advantages of AIMS is the ability to describe bond rearrangement. In Fig. 12 we show a sample of the kinds of reactive events that are observed in the simulations. Both panels show the time evolution of individual basis functions that are used to construct the time-dependent basis set. (Note that the time evolution of individual basis functions is not the same as the time evolution of expectation values. The two are equivalent only when only a single basis function is populated. In general, expectation values can be evaluated using the AIMS wavefunction and the appropriate operator.) The right and left panels originate (i.e., are spawned) from the same parent basis function (traveling on the excited electronic state), and this is a representative example in that one usually observes more than one reactive outcome from a particular parent basis function. In each panel, the time traces of the four C–H bond distances are shown, beginning when the depicted basis function is spawned from the excited state. The final products shown (in both panels) are transient, and they are expected to further decompose to acetylene. However, this decomposition occurs on a longer timescale, and only rarely have we observed

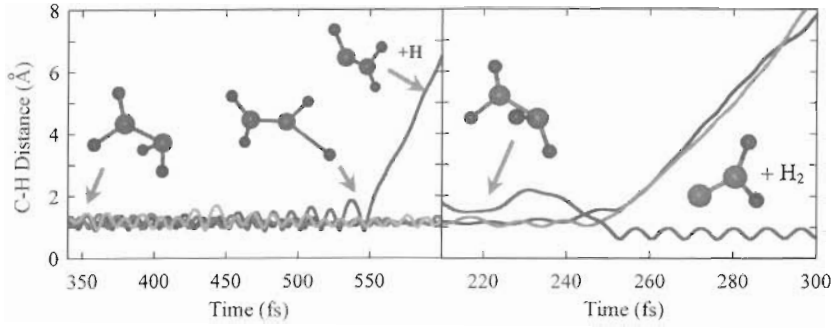

Figure 12. Sample of reactive outcomes of ethylene photochemistry. Right and left panels represent different basis functions (traveling on the ground electronic state) spawned from the same parent basis function (traveling on the excited electronic state) at different points in time. The final populations of the two basis functions are 56% and 15% (right and left panels, respectively). The time traces denote the four C–H bond distances as a function of time for the two (different) ground-state basis functions. Left panel: Formation of vinyl radical and atomic hydrogen. Right panel: Concerted elimination of molecular hydrogen and formation of vinylidene. Both products (vinyl radical and vinylidene) are expected to be transient, ultimately decomposing into acetylene. (Figure adapted from Ref. 215.)

acetylene formation within the simulation time window of 0.5 ps. This is not surprising, because there are significant barriers to be overcome from any of the transient photoproducts that we observe: vinyl radical, ethylidene, and vinylidene. Both calculation [168] and experiment [169] agree on a barrier of 1.66 eV for decomposition of vinyl radical to acetylene and atomic hydrogen. The barrier heights for decomposition of ethylidene and vinylidene are calculated [168,170,171] to be in the ranges 1.46–1.52 and 0.06–0.13 eV, respectively. Typically, bond rearrangement in our simulations occurs on the ground electronic state, but it is also observed much more rarely on the S_1 state. Experimental branching ratios between atomic and molecular hydrogen products, as well as molecular hydrogen internal and translational energy distributions, have been published [172–175]. Direct comparison to these experiments will require either longer simulation times or the use of statistical assumptions to extrapolate to $t = \infty$.

As a third and last example, we discuss the photodynamics of cyclobutene. The electrocyclic ring-opening reaction of cyclobutene (to 1,3-butadiene) is a classic example of a pericyclic rearrangement whose outcome is predicted by the Woodward–Hoffmann [176] (WH) rules and complementary theories [177–179]. The WH rules predict that for reactants containing $4n + 2$ π electrons the photochemical ring-opening reaction will proceed with disrotatory stereochemistry, while for reactants with $4n$ π electrons the photochemical ring opening will proceed in conrotatory fashion. For the case of cyclohexadiene,

this prediction (conrotatory) has been experimentally confirmed using both stereochemical analysis of the products in alkyl-substituted reactants [180–182] and resonance Raman spectroscopy [183,184]. Surprisingly, the results for the smaller cyclobutene (CB) molecule are less conclusive. Alkyl substitutions of CB have produced mixtures of allowed (disrotatory) and forbidden (conrotatory) photoproducts [185] and, because of controversies in the assignment of some bands, [186,187] the interpretation of resonance Raman experiments [188,189] (which provide a more direct probe of the excited-state dynamics) has been questioned. On the basis of the original assignment of the vibrational force field of CB [190], and a later assignment by Craig et al. [186], the resonance Raman spectrum [188] has been interpreted to show traces of a disrotatory ring opening [188,189]. However, based on their own assignment of the vibrational force field, and on their interpretation of the assignment of Wiberg and Rosenberg [187], Negri et al. [191] concluded that the resonance Raman spectrum does not show "any positive hint of the activity of distrotatory ring-opening motion."

The AIMS calculations used a HF-OA-CAS(4/4)*S wavefunction where the four active orbitals are those that become the two π orbitals in the butadiene photoproduct. Diffuse electronic basis functions were not included in the calculations. Therefore, we do not expect to reliably model those (long-time) features of the photochemistry and formation of ethylene, acetylene, and methylene-cyclopropane photoproducts [185,192] that are thought to arise from excitation to a low-lying $\pi \rightarrow 3s$ Rydberg state. Instead, our treatment focuses on the features that arise due to the state with the strongest oscillator strength: the $\pi \rightarrow \pi^*$ excited state. As in the case of ethylene, the excitation is assumed to be instantaneous and centered at the absorption maximum. Only four basis functions are used to describe the initial state, and we again use the AIMS-SP-SO method. Only short-time dynamics has been investigated (up to 50 fs), and during this short propagation time (and small set of initial conditions) we did not observe any nonadiabatic effects.

Figure 13 depicts a few snapshots of a typical excited-state trajectory, and we discuss the observed geometrical changes in chronological order. Following the electronic excitation the first motion is a stretching of the C=C bond. (Within 15 fs, the C=C bond extends by $\sim$0.4 Å.) This is expected for a $\pi \rightarrow \pi^*$ transition and is in agreement with the resonance Raman spectrum [188] that is dominated by the totally symmetric C=C stretching mode. An impulsive change in the hybridization of the methylenic carbons is also observed. As the CH_2–CH_2 bond breaks, the HCH angle changes from $\sim 109°$ (sp^3) to $\sim 120°$ (sp^2). The change in hybridization begins almost immediately after the electronic excitation and is completed within 50 fs. In the resonance Raman spectrum [188], this motion is manifested by a pronounced activity of the totally symmetric CH_2 scissors mode. Finally, and most importantly, Fig. 13

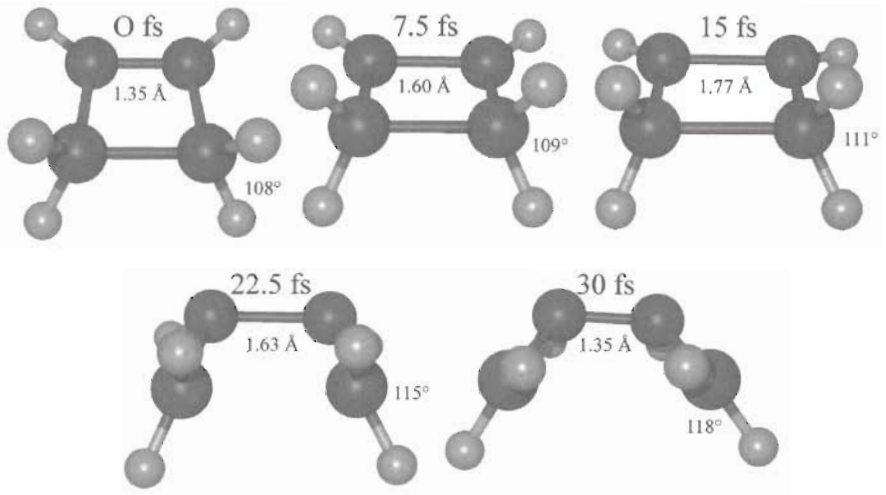

Figure 13. Snapshots of a typical excited state trajectory of cyclobutene. Values of the C–C bond distance and HCH hybridization angle are indicated. Immediately after the electronic excitation (at $t = 0$) the C–C bond begins to stretch. This is followed by a change in hybridization of the methylene carbons (from sp^3 to sp^2) and a pronounced disrotatory motion. (Figure adapted from Ref. 214.)

unambiguously shows that the excited-state dynamics are directed along the WH-predicted disrotatory reaction coordinate. In fact, this is the most pronounced feature observed in Fig. 13. In Fig. 14 we plot the absolute value of the average disrotatory angle as a function of time. The left inset of this panel defines the disrotatory coordinate, a coordinate that is *not* a normal mode of the molecule. (We plot the absolute value of the disrotatory angle because this motion can occur in two equivalent directions: Hydrogen atoms above/below the carbon skeleton rotate inward/outward or outward/inward.) The disrotatory motion begins shortly (approximately 10 fs) after the electronic excitation, and its amplitude is large (120°). No significant motion along the conrotatory reaction coordinate is observed. The right inset in the upper panel of Fig. 14 explains these observations. Here we show (solid line) a one-dimensional cut of the excited-state potential energy along the disrotatory and conrotatory coordinates (all other coordinates are kept at their ground-state equilibrium value). The Franck–Condon point on the excited electronic state remains a minimum with respect to conrotatory motion, but becomes unstable with respect to disrotatory motion. The dynamical conclusions we draw concerning the rapid onset of disrotatory motion arise largely because of the form of the excited state PES shown in the inset. Thus, we have also computed this cut (dashed line) using the MOLPRO program [193] with a larger cc-pVTZ basis set [194] and a

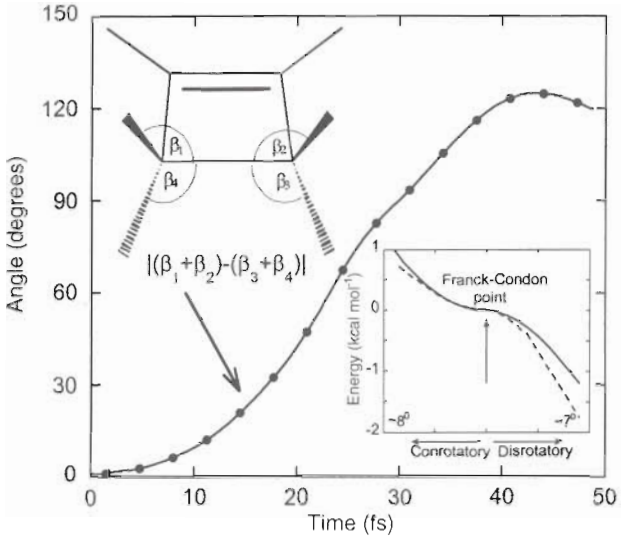

Figure 14. The absolute value of the average disrotatory angle as a function of time in femtoseconds. (The disrotatory angle is defined in the upper left inset.) Lower inset: A one-dimensional cut of the excited-state potential energy surface along the disrotatory and conrotatory coordinates. All other coordinates are kept at their ground-state equilibrium value, and the full and dashed lines correspond to two levels of electronic structure theory (see text for details). (Figure adapted from Ref. 216.)

more sophisticated electronic wavefunction (SA-3-CAS(4/4)*SD). The same qualitative behavior along the conrotatory and disrotatory coordinates is observed with this more accurate treatment of the electronic structure.

We now turn to the electronic structure during the dynamics. In Fig. 15 we show an isosurface rendition of the two frontier excited-state natural orbitals in the CI wavefunction. (At the beginning of the calculation these orbitals correspond most closely to π and π^* orbitals.) These are the natural orbitals of the basis function trajectory shown in Fig. 13. At early times (leftmost frames at 7.5 fs), before the onset of disrotatory motion, the excited-state wavefunction can be described using a single determinant with one electron in a π-like orbital (ϕ_a) and one in a π^*-like orbital (ϕ_b). During the disrotatory motion the character of the natural orbitals is more complicated and two determinants are required to describe the electronic wavefunction. In one determinant both electrons are in the ϕ_a orbital, and in the other they are both in the ϕ_b orbital. Both orbitals (ϕ_a and ϕ_b) show significant σ–π mixing which is expected due to the significant disrotatory motion. After the disrotatory motion is completed (rightmost frames at 22.5 fs), the excited-state wavefunction is again described

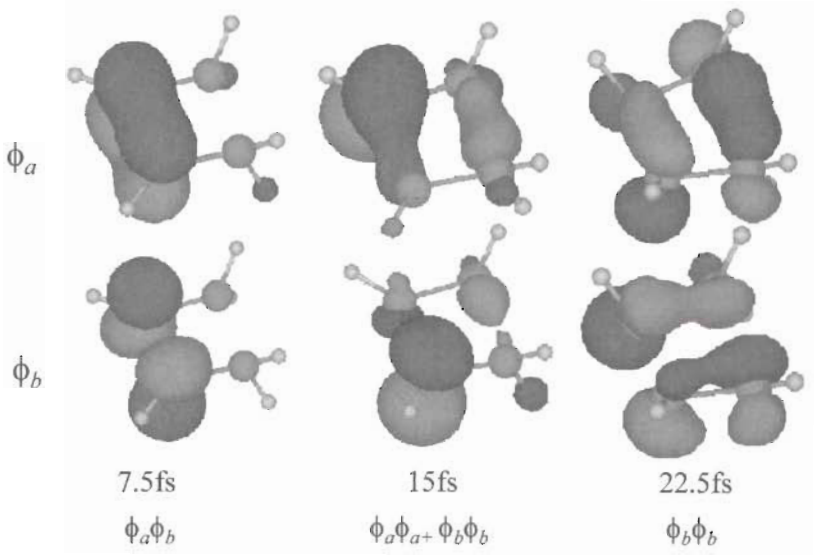

Figure 15. Snapshots of the two frontier excited-state natural orbitals (computed using the HF-OA-CAS(4/4)*S wavefunction) of the excited-state trajectory of cyclobutene shown in Fig. 13. Left panels: Before the onset of disrotatory motion, the excited-state wavefunction can be described using a single determinant with one electron in a π-like orbital (ϕ_a) and one in a π^*-like orbital (ϕ_b). Middle panels: During the disrotatory motion the simplest description of the electronic wavefunction requires two determinants. In one determinant both electrons are in the ϕ_a orbital, and in the other they are both in the ϕ_b orbital. Both orbitals (ϕ_a and ϕ_b) show significant σ–π mixing, which is a consequence of the significant disrotatory motion. Right panels: When the disrotatory motion is completed, the excited-state wavefunction is described by a single determinant in which both electrons are in the ϕ_b orbital. Note how the shape of the orbitals changes as the initial bonds are broken and the two new π bonds are formed.

using a single determinant. This time both electrons are in the ϕ_b orbital, which reflects the formation of the two new π bonds.

The interpretation of resonance Raman spectra is critically dependent on the assignment of the observed vibrational frequencies in the normal mode approximation. It is therefore crucial that the coordinate of interest correspond to a single normal mode and that the frequency of this normal mode be correctly assigned. In the case of CB, this has resulted in some controversy. The disrotatory motion is a non-totally symmetric coordinate (b_1 symmetry), projecting only on non-totally symmetric normal modes that may appear as odd overtones in the experimental spectra. Mathies and co-workers [188] observed an overtone of the 1075 cm^{-1} mode at 2150 cm^{-1}. Using the normal mode assignment of previous workers [186,190], they concluded that this mode is a non-totally symmetric CH_2 twist, projecting directly onto the disrotatory twist of the CH_2 groups. In 1995, this interpretation was challenged by Negri et al. [191]. They

revisited the normal mode analysis of CB and concluded, in agreement with a previous assignment by Wiberg and Rosenberg [187], that the 1075 cm^{-1} mode is mainly a CH_2 deformation (and not twist), while the lower-frequency 848 cm^{-1} mode is a CH_2 twist mode with a dominant disrotatory component. (Calculations of vibrational frequencies of d_2- and d_4-CB isotopomers provided further confirmation of their analysis.) This conflicting assignment of the CB normal modes led to the conclusion that the overtone at 2150 cm^{-1} does not provide any proof of disrotatory motion. Instead, Negri argued that the overtone of the 848 cm^{-1} mode would provide such proof. Unfortunately, one cannot determine if this overtone is present because of the intense band at 1650 cm^{-1}, which is attributed to butadiene photoproduct [188].

We have analyzed the character of the normal modes and agree with Negri et al. [191] that the assignment [186,190] on which Mathies [188] based his interpretation is incorrect. Although there is some component of disrotatory motion in the 1075 cm^{-1} normal mode, it is dominantly a CH_2 wag. Nevertheless, by following the excited-state dynamics we can conclude that the WH tendency is established during the first femtoseconds of the ring-opening. This suggests a role for impulsive character and kinematic effects on the efficacy of the WH rules for photochemical reactions. Indeed, one might then expect that classification of the cyclobutene and substituted cyclobutene ring-opening reactions that do and do not lead to the WH-predicted stereochemistry could be correlated with the effective mass of the substituents: The heavier the substituents, the more likely that the initial WH-directed impulse could be overcome by the detailed landscape of the excited-state potential energy surface. Further calculations and experiments—using, for example, deuterated cyclobutene—are needed to make progress in formulating such a theory.

B. Numerical Convergence

When judging the quality of the results produced by the AIMS method, it is important to distinguish the nuclear and electronic aspects; that is, one should test the accuracy of each one separately. Ideally one would like to demonstrate the convergence with a series of AIMS calculations following the usual quantum chemical hierarchy for the electronic structure part of the problem. However, computational limitations make this impractical at present. On the other hand, the more traditional time-independent approach of finding and characterizing special points on the PES will always require fewer PES evaluations than a time-dependent dynamical study. Hence, a higher level of electronic structure theory may be used in the time-independent case, and one can verify that the important features of the PESs remain consistent with the dynamical conclusions from an AIMS study. This has been done for the ethylene molecule, as discussed below. One of the main reasons for these extensive studies of the excited states of ethylene is the need to assess the role and importance of Rydberg states. Because

of computational limitations, the AIMS simulations were carried out with a double-ζ basis set. However, ethylene is known to possess many low-lying electronic states of Rydberg character; these cannot be reproduced without a more extensive basis set containing diffuse functions, and possibly also without a more detailed treatment of electron correlation.

Our high-level ethylene electronic structure calculations have used extended basis sets (aug-cc-pVDZ [195,196]) and state-averaged CASSCF wavefunctions. In some cases the orbitals determined from the SA-CASSCF have been used in an internally contracted multireference single and double-excitation configuration interaction treatment (MRSDCI) [197,198]. All the calculations used the MOLPRO [193] electronic structure code, and symmetry was never imposed on the electronic wavefunction. The calculations have followed the time ordering observed in the AIMS simulations, where one finds that immediately following the excitation the C–C bond stretches and subsequently the molecule begins to twist and pyramidalize. To investigate the extent of C–C bond stretching on the valence excited state (V state in Mulliken's notation), we have optimized the molecule under the constraint of a planar D_{2h} geometry. The formal reduction in the C–C bond order (the electronic excitation promotes an electron from a π orbital to a π^* orbital) is expected to result in stretching and twisting of this bond. The extent of this stretching is known to be sensitive to the amount of Rydberg-valence mixing in the V state. If this mixing is large, the extension is small because the delocalized nature of the Rydberg electrons leads these states to prefer only minor extension of the C–C bond. Previous theoretical studies [156] have found very slightly (≈ 0.05 Å) extended C–C bond lengths (for planar V-state ethylene). In contrast we find (using a SA-6-CAS(2,6)*SD wavefunction) significant stretching of the C–C bond by 0.139 Å. Furthermore, as the C–C bond is stretched, the ordering of the excited electronic states changes and the V state, which at the Franck–Condon geometry is the fourth excited state (S_4), becomes the third excited state (S_3) for $R_{CC} > 1.45$ Å. This significant stretching was also seen in the AIMS simulations that used considerably smaller basis sets (and less accurate wavefunctions).

The two panels in Fig. 16 show two-dimensional cuts of the PESs calculated using the OA-GVB-CAS(2/2)*S and SA-3-CAS(2/6)*SD wavefunctions (in the latter case the aug-cc-pVDZ basis set was used). At both levels of theory the twisted geometry of ethylene (D_{2d} symmetry) is not a true minimum, but rather a saddle point. This is at variance with previous studies at lower levels of theory [18], but in agreement with our AIMS results. The lowest points on the S_1 PES are conical intersections, not true minima. Of these, we have found two nearly isoenergetic intersections: (a) the twisted/pyramidalized geometry that the AIMS simulations also highlighted and (b) another that corresponds to ethylidene. A third type of intersection involving hydrogen migration is similar to the

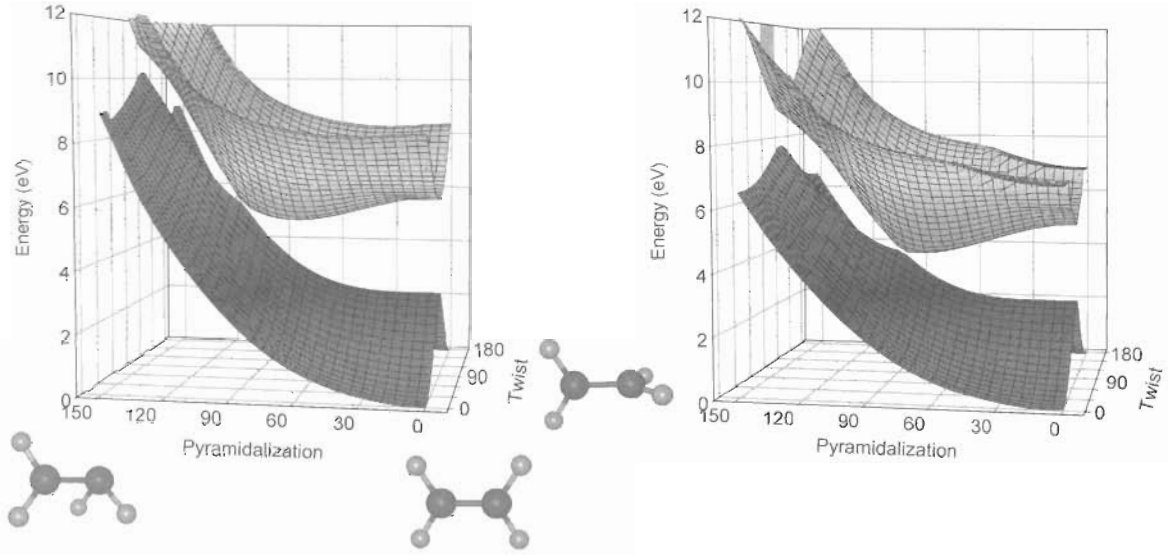

Figure 16. Left panel: The ground and first excited electronic states of ethylene, computed using the OA-GVB-CAS(2/2)*S wavefunction, as a function of the pyramidalization and twist angles. (All other coordinates, except the C–C bond distance, are kept at their ground-state equilibrium value and the C–C bond distance is stretched to 1.426 Å.) On the ground electronic state the molecule is planar (twist angle 0° or 180°), and on the lowest excited state the twisted geometry (twist angle 90°) is a saddle point. Accessing the conical intersection requires pyramidalization of one of the methylene fragments. Right panel: Same as left panel but computed using the aug-cc-pVDZ basis set and a three-state-averaged CAS(2/6) wavefunction augmented with single and double excitations, that is, SA-3-CAS(2/6)*SD. The form of the excited-state PES is in agreement with the simpler model of the left panel; in particular, the lowest energy point on the lowest excited state remains pyramidalized. (Figure adapted from Ref. 214.)

one found by Ohmine [199]. This intersection is not a minimal energy point on the intersection seam but is energetically accessible after photoexcitation. Our AIMS simulations find that it does not usually lead to efficient $S_1 \rightarrow S_0$ quenching, possibly because of PES topography (cf. the $Li+H_2$ example discussed above.) An intersection between the valence and ionic states (V and Z) was also identified. This intersection was not seen in the AIMS simulations, most of which were restricted to include only S_0 and S_1 states.

Near the equilibrium geometry of ground-state ethylene, the first three low-lying excited states are Rydberg states, while at the photochemically important geometries (e.g., twisted, pyramidalized) the lowest excited state has purely valence character and the Rydberg states are higher in energy. As a consequence, the excited molecule must first descend through the manifold of Rydberg states before it can decay back to the ground electronic state. The torsion angle can facilitate this by stabilizing the valence states and destabilizing the Rydberg states. We have investigated this cascade of conical intersections using a SA-2-CAS(2,6) wavefunction. First, we located the intersection between the valence state (S_4) and the adjacent Rydberg state (S_3). Once this intersection was located (in the proximity of the planar geometry), we computed a one-dimensional cut along the twist coordinate, keeping all other coordinates at their values at the S_4/S_3 crossing. In Fig. 17 we show the resulting cascade of valence/Rydberg conical intersections. As the molecule is twisted, the energy of the Rydberg states increases while that of the valence state decreases. The molecule must twist by $\sim 60^\circ$ to leave the manifold of Rydberg states. The energy of the ionic (Z) state begins to decrease at larger twist angles, and at the 90°-twisted geometry, this state is strongly coupled to the valence state (as evidenced by the strong avoided crossing at $\sim 80^\circ$).

Overall the results of high-level electronic structure studies confirm the features of the excited state PESs that lead to the photodynamics observed in the AIMS simulations. However, they also highlight the valence/Rydberg conical intersections that exist in ethylene. It would be interesting to characterize the dynamics as the molecule descends through the manifold of Rydberg states (which were not included in our dynamical simulations). *A priori*, it is not clear to what extent the dynamics will be diabatic—that is, to what extent the Rydberg states are just spectators in the dynamics. More detailed AIMS simulations that treat the Rydberg states properly and allow for coupling of up to six electronic states are planned to address this issue.

When the FMS method was first introduced, a series of test calculations were performed using analytical PESs. These calculations tested the numerical convergence with respect to the parameters that define the nuclear basis set (number of basis functions and their width) and the spawning algorithm (e.g., λ_0 and MULTISPAWN). These studies were used to validate the method, and therefore we refrained from making any approximations beyond the use of a

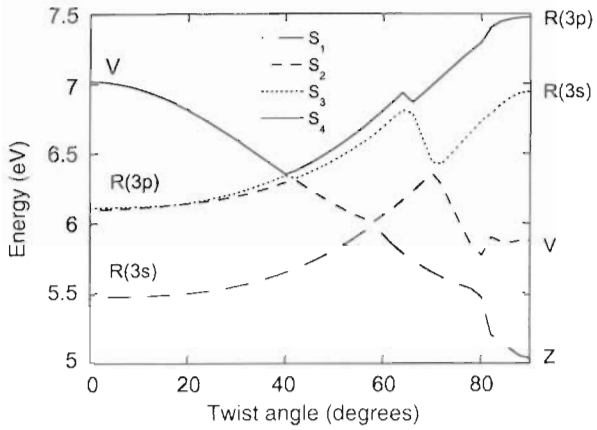

Figure 17. The four lowest excited electronic states of ethylene, computed using the SA-6-CAS(2/6) wavefunction (and the aug-cc-pVDZ basis set), as a function of the twist angle. All other coordinates are kept at their values at the first crossing between S_4 (full line) and S_3 (dotted line): $R_{CC} = 1.3389$ Å, $R_{CH} = 1.128$ Å, and $\angle HCH = 112.1°$. The four states are labeled using both adiabatic (S_1, S_2, S_3, and S_4) and diabatic [V, Z, R(3*s*) and R(3*p*)] notations. At the planar geometry (twist angle is 0°) the first three excited states are Rydberg states and S_4 is the V state. As the molecule is twisted, the Rydberg states are destabilized while the V state is stabilized. This results in a cascade of V/R conical intersections. A twist angle of $\sim 60°$ is required to leave the manifold of Rydberg states completely. As the molecule is twisted further, the energy of the ionic state (Z) decreases, and this state is strongly coupled to the valence (V) state at the 90°-twisted geometry. (Figure adapted from Ref. 33.)

finite basis set. Using a set of one-dimensional problems introduced by Tully [96], we first showed that the method is capable of reproducing exact (numerically converged) quantum results with a small number of basis functions [38]. These one-dimensional tests may seem trivial (to us as well as to the readers), but the important conclusion is not the ability to reproduce exact results but rather the ability to do this with a small number of basis functions—typically less than 10 for these one-dimensional cases. This provided the first empirical evidence for the underlying assumption of the AIMS method, namely that the basis set expansion could converge quickly if classical mechanics provided a good zeroth-order picture. The next set of tests used a two-dimensional, two-electronic-state problem [40,41]. We intentionally chose a model that avoided harmonic and/or separable PESs. In this two-dimensional avoided crossing model, shown in Fig. 1, each of the two diabatic surfaces describes a collinear nonreactive collision between an atom and a diatomic molecule, and the interstate coupling is set to a constant. One diabatic potential corresponds to an $A + BC$ arrangement, and the other corresponds to $AB + C$. The corresponding ground- and excited-state adiabatic potentials describe a reactive atom

exchange reaction and a bound linear triatomic molecule, respectively. We used a Morse oscillator for the AB (BC) vibration and an exponentially repulsive form for the A–B (B–C) interaction. All three atoms were taken to be identical; and force constants, anharmonicities, and masses were chosen according to spectroscopic information for Li_2. The PESs are highly anharmonic, and both degrees of freedom are strongly coupled. All the calculations were carried out in the diabatic representation, and the required matrix elements were evaluated analytically. We studied a broad range of relative kinetic energies (atom with respect to center of mass of diatomic molecule) beginning at the ground-state adiabatic barrier and ending at an energy above the bottom of the excited state well. The initial nuclear wavefunction was centered in the asymptotic region (atom far from the molecule which is in the ground vibrational state), and 30 basis functions were used to represent the initial state. Using this initial basis set, quantitative agreement in expectation values and branching ratios for this broad range of energies was demonstrated. Convergence with respect to the initial size of the basis set was investigated by repeating the calculations using 10 and 20 initial basis functions (all other parameters—e.g., λ_0 and MULTI-SPAWN—were kept the same). The final branching ratios were found to gradually converge to the exact value as the size of the basis increased from 10 to 20 and then 30, and the overall time dependence of the transmission probability was already reproduced with only 10 initial basis functions.

The same two-dimensional two-electronic-state model was used to test the TDB algorithm. All the parameters were kept as before, but instead of using 30 independent initial conditions we chose 10 independent initial conditions ($N_s = 10$) and augmented the basis set to 30 by displacing each initial condition forward and backward in time. The displacements should not be too small (basis functions become linearly dependent) or too large (basis functions become uncoupled). Given these considerations, we did not specify the amount of time for displacement, but rather displaced the basis functions so that the overlap between any two neighboring basis functions that belong to the same seed is $\sim$0.7. For an initial state that is represented by 10 independent (and 20 time-displaced) basis functions versus 30 independent basis functions, the reduction in computational cost is almost a factor of two. Achieving this reduction in computational effort does carry a penalty: Matrix elements that will be reused must be stored. For each seed (10 in this case), all the matrix elements at each point in time between the forward-most and backward-most displaced basis functions should be stored. The total number of matrix elements to be stored is therefore given by the product of the number of new matrix element evaluations (255 in this example) and the number of time points between the forward-most and backward-most basis functions, N_t. In the present case, which we expect to be quite typical, the average value of N_t was approximately 20, and therefore the memory requirement was modest. In general, the extra storage requirement

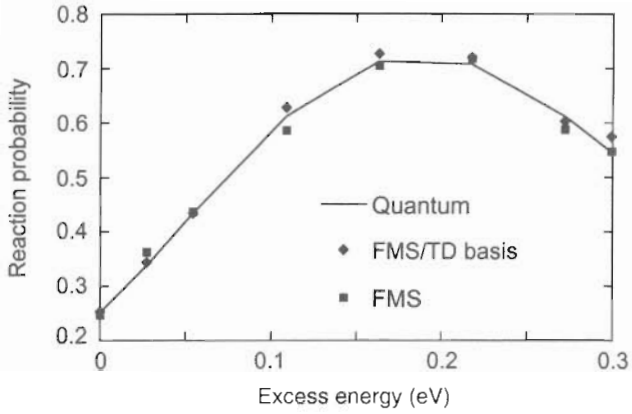

Figure 18. Diabatic reaction probability as a function of excess energy in eV for the collinear A + BC → AB + C model shown in Fig. 1. (Excess energy is measured relative to the barrier height of the ground-state adiabatic potential energy surface.) Full line: Exact quantum mechanical results. Diamonds: Multiple-spawning with a time-displaced basis set. Squares: multiple-spawning with a regular basis set. All three calculations are in the diabatic representation, and the range of energies shown begins at the ground-state adiabatic potential energy barrier and extends to an energy above the bottom of the excited-state adiabatic well. (Figure adapted from Ref. 41.)

scales as $O(N_s^2 + N_s N)$, which is insignificant compared to the Hamiltonian matrix itself.

Figure 18 depicts the diabatic reaction probability ($P_{1\to 2} = A + BC \to AB + C$) as a function of the excess energy for the TDB (diamonds), regular basis set (squares), and numerically exact (full line) methods. (The excess energy is defined as the difference between the initial relative kinetic energy and the barrier height in the adiabatic ground-state potential energy surface; cf. Fig. 4 in Ref. 40.) The agreement between the TDB results and the numerically exact results is very good throughout the energy range shown, and, more importantly, the results of the multiple-spawning method do not change when the TDB is used. Similar agreement is also obtained for expectation values as a function of time.

For this and other problems, the spread in the results depends on the initial size of the basis set. For small basis sets, the final branching ratios depend on the initial conditions—position and momentum parameters that define each basis function. Because in the TDB only 10 (out of 30) initial conditions were chosen independently, it is instructive to compare its results to the ones obtained when only 10 independent basis functions are used to represent the initial wavefunction. The purpose of this comparison is to examine the dependence of the branching ratios on the initial conditions and not to demonstrate an improvement in the results. Such an improvement is expected because the

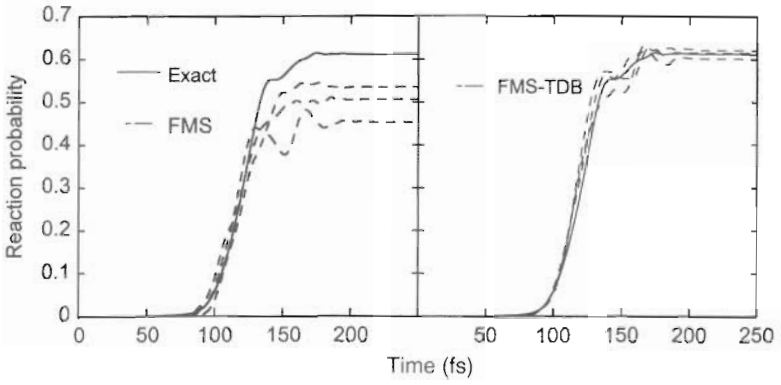

Figure 19. Diabatic reaction probability as a function of time (in femtoseconds) for the collinear A + BC → AB + C model of Fig. 1, at an excess energy of 0.109 eV. In both panels, the full line designates the exact quantum mechanical results and the dashed lines are multiple spawning results with different initial conditions. Right panel: TDB using an initial basis set with 30 basis functions and 10 seeds. Left panel: Regular basis set using an initial basis set with 10 basis functions. (Figure adapted from Ref. 41.)

computational effort increases when 10 independent basis functions are augmented with 20 TDB functions. This comparison is shown in Fig. 19. In both panels, the full line designates the numerically exact results and the dashed lines designate three different runs of the regular multiple spawning (left panel) and the TDB version (right panel). The TDB results are clearly converged, whereas the ones without the TDB functions are not (i.e., they depend on the initial conditions).

The results of this test of the TDB-FMS method are encouraging, and we expect the gain in efficiency to be more significant for larger molecules and/or longer time evolutions. Furthermore, as noted briefly before, the approximate evaluation of matrix elements of the Hamiltonian may be improved if we can further exploit the temporal nonlocality of the Schrödinger equation.

In the past decade, vibronic coupling models have been used extensively and successfully to explain the short-time excited-state dynamics of small to medium-sized molecules [200–202]. In many cases, these models were used in conjunction with the MCTDH method [203–207] and the comparison to experimental data (typically electronic absorption spectra) validated both the MCTDH method and the model potentials, which were obtained by fitting high-level quantum chemistry calculations. In certain cases the *ab initio*-determined parameters were modified to agree with experimental results (e.g., excitation energies). The MCTDH method assumes the existence of factorizable parameterized PESs and is thus very different from AIMS. However, it does scale more favorably with system size than other numerically exact quantum

dynamics techniques (e.g., pseudospectral Fourier methods). Therefore, the availability of the MCTDH method and its application to vibronic coupling models provide a unique opportunity to compare FMS and numerically converged quantum dynamics for problems of large dimensionality (e.g., up to 24 degrees of freedom). Vibronic coupling model Hamiltonians are constructed using the mass-weighted ground-state normal modes, **Q**, and the diabatic representation. They typically contain (i) a term that describes the ground-state Hamiltonian in the diabatic representation, (ii) a matrix of state energies, (iii) linear on-diagonal expansion terms, (iv) linear off-diagonal coupling terms, (v) quadratic and bilinear diagonal terms, and (vi) bilinear off-diagonal terms. The first four terms appear in all vibronic coupling models, while the last two occur only when the Hamiltonian is expanded to second order. As a test case for the FMS method, we have chosen the electronic absorption spectrum of pyrazine. Various model Hamiltonians have been developed for this system, enabling tests of the FMS method using three- [208], four- [209], and 24-dimensional [202] model Hamiltonians. Both the three- and four- dimensional Hamiltonians used here include only linear coupling terms, while the 24-dimensional one includes also quadratic on- and off-diagonal coupling terms. The 24-dimensional Hamiltonian is discussed in detail in Ref. 202, and hence for simplicity here we only write the simpler three- and four-dimensional ones explicitly:

$$\mathbf{H} = \begin{bmatrix} H_0 - \Delta + \sum_i \kappa_i^1 Q_i & \lambda Q_{10a} \\ \lambda Q_{10a} & H_0 + \Delta + \sum_i \kappa_i^2 Q_i \end{bmatrix} \tag{3.1}$$

In Eq. (3.1), H_0 is a three- or four- dimensional harmonic oscillator Hamiltonian

$$H_0 = \sum_i \frac{\omega_i}{2} \left(-\frac{\partial^2}{\partial Q_i^2} + Q_i^2 \right) \tag{3.2}$$

Δ is the energy of the state (i.e., 2Δ is the energy difference between the two electronic states), κ_i^j are the gradients of the excitation energy with respect to the normal coordinate Q_i at the reference geometry, and λ is the vibronic-coupling constant. In the case of pyrazine, the two electronic states are $S_1[^1B_{3u}(n\pi^*)]$ and $S_2[^1B_{2u}(\pi\pi^*)]$, and only the totally symmetric ν_{10a} vibrational mode can couple these two states. The other, non-totally symmetric modes are ν_1 and ν_{6a} for the three-dimensional model and ν_1, ν_{6a}, and ν_{9a} for the four-dimensional one. The parameters for the three- and four-dimensional models are listed in Tables I and II, and those for the 24-dimensional model are listed in Ref. 202. For the three- and four-dimensional models, numerically converged results were obtained using the Newton interpolation formula [45] and Fourier techniques, [44]; and for the 24-dimensional model, (nearly) numerically converged results were obtained using version 8 of the MCTDH program [210]. In all cases the

TABLE I
Parameters for the Three Dimensional S_1-S_2 Vibronic Coupling Model of Pyrazine [208]. All Quantities are in eV

	ω	κ^1	κ^2	λ	Δ
ν_1	0.126	0.037	−0.254		
ν_{6a}	0.074	−0.105	0.149		
ν_{10a}	0.118			0.262	
					0.450

calculations were performed in the diabatic representation. This representation is advantageous because all the required integrals can be evaluated analytically, but there is a penalty for using it. In the diabatic representation, the coupling between the two states is broad and in particular it is nonnegligible in the Franck–Condon region, implying that when we begin the simulation the system is already in a nonadiabatic region. As a consequence, a large number of basis functions are spawned and the spawning should begin before the actual simulation begins. To overcome the second problem we "pre-spawn" basis functions on the initially unpopulated electronic state (S_1 in this case). After selecting initial conditions for the basis functions on the S_2 state (these were chosen from the Wigner transform of the ground vibrational wavefunction on S_0), a mirror basis, with the same position and momentum parameters, was placed on the S_1 state. None of these ("virtual") basis functions on the S_1 state were populated at $t = 0$; however, once the simulation started, their amplitudes quickly changed. In order to control the number of basis functions spawned, we have (1) set an upper limit (of 900) on the size of the nuclear basis set (i.e., once the number of basis functions on both electronic states reaches 900, spawning is no longer allowed regardless of the magnitude of the nonadiabatic coupling) and (2) ramped the spawning threshold λ_0 during the propagation (i.e., the magnitude of λ_0 and λ_f increases as a function of time). (Option 1 was always used, whereas 2

TABLE II
Parameters for the Four Dimensional S_1-S_2 Vibronic Coupling Model of Pyrazine [209]. All Quantities are in eV

	ω	κ^1	κ^2	λ	Δ
ν_1	0.12730	0.0470	0.2012		
ν_{6a}	0.07400	−0.0964	0.1194		
ν_{9a}	0.15680	0.1594	0.0484		
ν_{10a}	0.09357			0.1825	
					0.46165

was enforced in only some of the calculations.) In all the three-, four-, and 24-dimensional calculations, the size of the initial basis set (on each electronic state) was 20, 40, and 60, respectively, and only the S_2 state was populated at $t = 0$. The comparison to the exact methods (Fourier or MCTDH) focuses on the electronic absorption spectrum. The absorption spectrum obtained using MCTDH for the 24-dimensional model Hamiltonian has been shown to be in good agreement with the experimentally measured one. Certain aspects of this class of models are more challenging than our previous tests—high dimensionality and existence of conical intersections. Other aspects are not; the zeroth-order Hamiltonian is harmonic.

The three panels of Fig. 20 compare the FMS and numerically exact electronic absorption spectra. For the three- and four-dimensional models, the FMS method reproduces both the width of the spectrum and its finer features (location and intensity of the various peaks) very well. For the 24-dimensional model, the agreement in the width is good but the finer details are not reproduced as well as for the lower-dimensionality models. Presumably this is a consequence of the relatively small size of the nuclear basis set. It is quite possible that, in the case of a 24-dimensional model, the basis set is too small to correctly describe the spreading of the wavepacket. In Ref. 211, the convergence of the FMS method as a function of the initial basis set size and spawning threshold is discussed in detail, and here we only make a few comments. As the spawning threshold is increased, fewer basis functions are spawned and therefore the results gradually deteriorate. In the case of the three-dimensional model, the rate at which the results deteriorate is quite slow as demonstrated in Fig. 21. The exact results are compared to FMS results with very different spawning thresholds, from 2.5 to 20 atomic units. In all cases the envelopes of the FMS and exact absorption spectra are in good agreement. However, the details of the spectrum are not reproduced when the spawning threshold is increased. As might be expected, the short-time behavior of the wavefunction which gives rise to the spectral envelope is less sensitive to the spawning threshold.

IV. OUTLOOK AND CONCLUDING REMARKS

In many chemical and even biological systems the use of an *ab initio* quantum dynamics method is either advantageous or mandatory. In particular, photochemical reactions may be most amenable to these methods because the dynamics of interest is often completed on a short (subpicosecond) timescale. The AIMS method has been developed to enable a realistic modeling of photochemical reactions, and in this review we have tried to provide a concise description of the method. We have highlighted (a) the obstacles that should be overcome whenever an *ab initio* quantum chemistry method is coupled to a quantum propagation method, (b) the wavefunction ansatz and fundamental

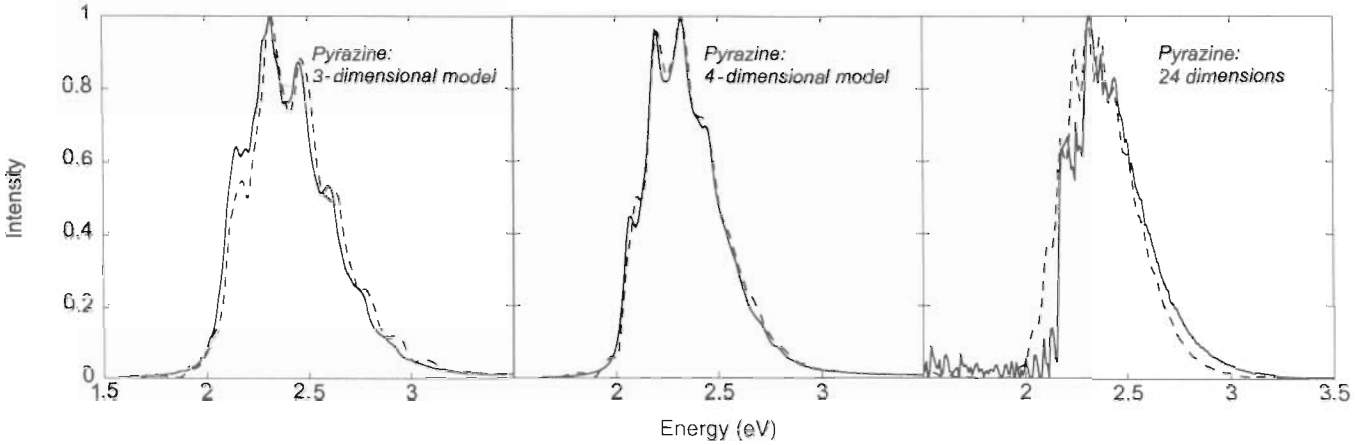

Figure 20. The ($S_0 \rightarrow S_2$) absorption spectrum of pyrazine for reduced three- and four-dimensional models (left and middle panels) and for a complete 24-vibrational model (right panel). For the three- and four-dimensional models, the exact quantum mechanical results (full line) are obtained using the Fourier method [43,45]. For the 24-dimensional model (nearly converged), quantum mechanical results are obtained using version 8 of the MCTDH program [210]. For all three models, the calculations are done in the diabatic representation. In the multiple spawning calculations (dashed lines) the spawning threshold (λ_0) is set to 0.05, the initial size of the basis set for the three-, four-, and 24-dimensional models is 20, 40, and 60, and the total number of basis functions is limited to 900 (i.e., regardless of the magnitude of the effective nonadiabatic coupling, we do not spawn new basis functions once the total number of basis functions reaches 900).

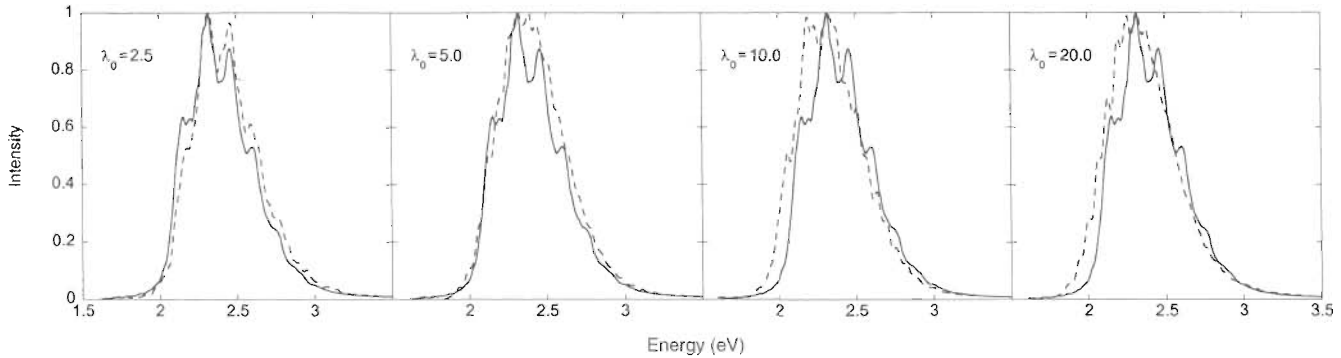

Figure 21. The ($S_0 \rightarrow S_2$) absorption spectrum of pyrazine for the reduced three-dimensional model using different spawning thresholds. Full line: Exact quantum mechanical results. Dashed line: Multiple spawning results for $\lambda_0 = 2.5$, 5.0, 10, and 20. (All other computational details are as in Fig. 20.) As the spawning threshold is increased, the number of spawned basis functions decreases, the numerical effort decreases, and the accuracy of the result deteriorates (slowly). In this case, the final size of the basis set (at $t = 0.5$ ps) varies from 860 for $\lambda_0 = 2.5$ to 285 for $\lambda_0 = 20$.

equations of the AIMS method, (c) required and optional approximations, (d) the analysis of the results, and (e) some advanced topics that are not required for a basic understanding of the method. The accuracy of the AIMS and FMS methods has been discussed. When the FMS method was first introduced, its accuracy (and computational efficiency) was tested using simple one- and two-dimensional problems. More recently, these tests have been extended to larger systems of three, four, and 24 dimensions. In this review we have discussed only the latter set of tests, because the older, and to some extent easier, tests have been extensively discussed in past publications. The applications section showed that it is indeed possible to model photochemical reactions from first principles for molecules of general chemical interest.

Throughout the review we have emphasized possible directions for improvements and extensions. There is considerable room for improvement in our treatment of both the electronic structure and nuclear dynamics—in certain cases with minimal increase in computational effort. Consider first the electronic structure and the case of ethylene. The electronic structure treatment that we have used does not do full justice to the Rydberg states of the molecule. We are currently exploring the role of the Rydberg states by carrying out calculations on ethylene with more extended basis sets; while computationally tractable, these calculations are quite challenging. Certainly, such studies on cyclobutene and butadiene, while of great interest to us, are not yet possible. While the ever-increasing speed of computers will likely make these possible in the near future, there is a clear need to implement analytical gradients in our calculations and also for new approaches to the electronic structure of excited states. Time-dependent density functional theory is one promising avenue. Others include combinations of interpolation and direct dynamics strategies, as well as hybrid quantum mechanical/classical electrostatic models of potential energy surfaces. The latter direction is currently being implemented and the hybrid interpolation/direct dynamics strategy has already been implemented (for a triatomic system) as discussed in Section III.A.

Similarly, improvement in the accuracy of the nuclear dynamics would be fruitful. While in this review we have shown that, in the absence of any approximations beyond the use of a finite basis set, the multiple spawning treatment of the nuclear dynamics can border on numerically exact for model systems with up to 24 degrees of freedom, we certainly do not claim this for the *ab initio* applications presented here. In principle, we can carry out sequences of calculations with larger and larger nuclear basis sets in order to demonstrate that experimentally observable quantities have converged. In the context of AIMS, the cost of the electronic structure calculations precludes systematic studies of this convergence behavior for molecules with more than a few atoms. A similar situation obtains in time-independent quantum chemistry—the only reliable way to determine the accuracy of a particular calculation is to perform a sequence of

calculations in a hierarchy of increasing basis sets and electron correlation. What is critically different about time-independent quantum chemistry is that well-defined and extensively tested hierarchies exist—for example, the correlation consistent basis sets of Dunning and co-workers [194,196,212] and the increasing orders of perturbation theory, MPn [213]. Developing such hierarchies for the FMS method is an important goal that is prerequisite to the widespread use of AIMS. We are working toward this goal, but it is important to recognize that it will only be useful if it arises from an extensive set of applications. It is not fruitful to propose a computational hierarchy unless the incremental improvements going from one step to the next are similar throughout, and at the present stage it appears that this can only be determined empirically.

Practical use of the AIMS method requires certain approximations (see Section II.D) with the most severe being the use of a first-order saddle point approximation for the Hamiltonian (diagonal and off-diagonal) matrix elements. Even in the case of predetermined analytical potential energy surfaces, this approximation is required if the matrix elements of the Hamiltonian cannot be evaluated analytically. When the SP approximation was first introduced, its accuracy was tested [74]. Although the results were favorable, more rigorous tests using an extensive set of applications/models should be performed. Also, as discussed in Section II.D, the current implementation of the SP approximation is wasteful. Although we have information about the PESs for all possible pairs of nuclear basis functions (populated or not), individual matrix elements of the Hamiltonian (each involving one pair of basis functions) are evaluated using only a single data point (i.e., one relevant pair of basis functions). If the proper weighting scheme for all the other data points were developed, we could improve the accuracy of the SP approximation without any increase in computational expense. Additional increase in accuracy, again without increasing computational cost, could be obtained by incorporating information about the PESs from previous time-points in the calculation. Preliminary attempts in this direction have been discussed in Section II.F, but clearly much more can and should be done.

We hope that we have convinced the reader that, even though significant improvements can be expected in the future, the AIMS method is currently practical and useful for problems that are of chemical interest. In the near future we expect to be able to handle condensed phase and biological systems. This will open a new challenging and exciting area for applications of *ab initio* quantum dynamics.

Acknowledgments

We began to work on the AIMS method under the guidance of Professor R. D. Levine. We are grateful for his insight, knowledge, and enthusiasm. We would like to thank Dr. G. Ashkenazi for providing us his efficient and elegant Fourier propagation and Wigner transform codes.

Dr. K. Thompson has taught us about interpolation methods. It was a pleasure to work with him on the hybrid interpolation/*ab initio* AIMS method. J. Quenneville diligently worked with us on the photochemistry of ethylene, and we greatly appreciate his contributions. The MCTDH program enabled us to extensively test our method. We thank Professor H.-D. Meyer for providing the program and promptly answering all our questions about it. Dr. L. Murga contributed to the initial coding of the vibronic coupling models. Professor D. G. Truhlar and Dr. M. Hack have presented us with new challenging tests for the FMS method (not presented here) and have engaged us in stimulating discussions about semiclassical and surface-hopping dynamics. Financial support for this work was provided by the U.S. Department of Energy through the University of California under Subcontract No. B341494, the National Science Foundation (CHE-97-33403), and the National Institutes of Health (PHS-5-P41-RR05969). TJM is the grateful recipient of CAREER, Research Innovation, Beckman Young Investigator, and Packard Fellow awards from NSF, Research Corporation, The Beckman Foundation, and the Packard Foundation, respectively.

References

1. C. Leforestier, *J. Chem. Phys.* **68**, 4406 (1978).
2. R. Car and M. Parrinello, *Phys. Rev. Lett.* **55**, 2471 (1985).
3. M. Parrinello, *Solid State Comm.* **102**, 107 (1997).
4. R. Car and M. Parrinello, *NATO ASI Ser., Ser. B* **186**, 455–476 (1989).
5. D. K. Remler and P. A. Madden, *Mol. Phys.* **70**, 921 (1990).
6. M. E. Tuckerman, P. J. Ungar, T. Vonrosenvinge, and M. L. Klein, *J. Phys. Chem.* **100**, 12878–12887 (1996).
7. M. C. Payne, M. P. Teter, D. C. Allan, T. A. Arias, and J. D. Joannopoulos, *Rev. Mod. Phys.* **64**, 1045 (1992).
8. B. Hartke and E. A. Carter, *Chem. Phys. Lett.* **189**, 358 (1992).
9. B. Hartke and E. A. Carter, *J. Chem. Phys.* **97**, 6569–6578 (1992).
10. Z. Liu, L. E. Carter, and E. A. Carter, *J. Phys. Chem.* **99**, 4355–4359 (1995).
11. S. Hammes-Schiffer and H. C. Andersen, *J. Chem. Phys.* **99**, 523 (1993).
12. S. A. Maluendes and M. Dupuis, *Int. J. Quant. Chem.* **42**, 1327 (1992).
13. J. Jellinek, V. Bonacic-Koutecky, P. Fantucci, and M. Wiechert, *J. Chem. Phys.* **101**, 10092 (1994).
14. M. Klessinger and J. Michl, *Excited States and Photochemistry of Organic Molecules*, VCH Publishers, New York, 1995.
15. M. Garavelli, F. Bernardi, M. Olivucci, T. Vreven, S. Klein, P. Celani, and M. A. Robb, *Faraday Disc.* **110** (1998).
16. R. Ditchfield, J. E. Del Bene, and J. A. Pople, *J. Am. Chem. Soc.* **94**, 703 (1972).
17. J. B. Foresman, M. Head-Gordon, J. A. Pople, and M. J. Frisch, *J. Phys. Chem.* **96**, 135–149 (1992).
18. K. B. Wiberg, C. M. Hadad, J. B. Foresman, and W. A. Chupka, *J. Phys. Chem.* **96**, 10756 (1992).
19. R. Singh and B. M. Deb, *Phys. Rep.* **311**, 47–94 (1999).
20. I. Frank, J. Hutter, D. Marx, and M. Parrinello, *J. Chem. Phys.* **108**, 4060–4069 (1998).
21. K. Yabana and G. F. Bertsch, *Int. J. Quantum. Chem.* **75**, 55 (1999).
22. K. K. Docken and J. Hinze, *J. Chem. Phys.* **57**, 4928 (1972).
23. H.-J. Werner and W. Meyer, *J. Chem. Phys.* **74**, 5794 (1981).
24. H.-J. Werner and W. Meyer, *J. Chem. Phys.* **74**, 5802 (1981).

25. B. H. Lengsfield III and D. R. Yarkony, *Adv. Chem. Phys.* **82**, 1 (1992).
26. H. F. Schaefer and C. F. Bender, *J. Chem. Phys.* **55**, 1720 (1971).
27. P. J. Hay, T. H. Dunning, Jr., and W. A. Goddard III, *J. Chem. Phys.* **62**, 3912–3924 (1975).
28. M. J. S. Dewar, J. A. Hashmall, and C. G. Venier, *J. Am. Chem. Soc.* **90**, 1953–1957 (1968).
29. A. I. Krylov, *Chem. Phys. Lett.* **338**, 375–384 (2001).
30. E. R. Davidson, *J. Phys. Chem.* **100**, 6161 (1996).
31. W. A. Goddard III, T. H. Dunning, Jr., W. J. Hunt, and P. J. Hay, *Acc. Chem. Res.* **6**, 368–376 (1973).
32. M. Ben-Nun and T. J. Martínez, *Chem. Phys. Lett.* **298**, 57 (1998).
33. M. Ben-Nun and T. J. Martínez, *Chem. Phys.* **259**, 237 (2000).
34. K. Ruedenberg and G. J. Atchity, *J. Chem. Phys.* **99**, 3799 (1993).
35. W. Domcke and C. Woywod, *Chem. Phys. Lett.* **216**, 362 (1993).
36. C. Galloy and J. C. Lorquet, *J. Chem. Phys.* **67**, 4672 (1977).
37. R. Cimiraglia, M. Persico, and J. Tomasi, *Chem. Phys.* **53**, 357 (1980).
38. T. J. Martínez, M. Ben-Nun, and R. D. Levine, *J. Phys. Chem.* **100**, 7884 (1996).
39. T. J. Martínez, M. Ben-Nun, and R. D. Levine, *J. Phys. Chem.* **101A**, 6389 (1997).
40. M. Ben-Nun and T. J. Martínez, *J. Chem. Phys.* **108**, 7244 (1998).
41. M. Ben-Nun and T. J. Martínez, *J. Chem. Phys.* **110**, 4134 (1999).
42. E. J. Heller, *J. Chem. Phys.* **62**, 1544 (1975).
43. D. Kosloff and R. Kosloff, *J. Comp. Phys.* **52**, 35 (1983).
44. R. Kosloff, *Annu. Rev. Phys. Chem.* **45**, 145 (1994).
45. G. Ashkenazi, R. Kosloff, S. Ruhman, and H. Tal-Ezer, *J. Chem. Phys.* **103**, 10005 (1995).
46. E. J. Heller, *J. Chem. Phys.* **75**, 2923 (1981).
47. D. J. Tannor and E. J. Heller, *J. Chem. Phys.* **77**, 202 (1982).
48. E. J. Heller, R. L. Sundberg, and D. Tannor, *J. Phys. Chem.* **86**, 1822 (1982).
49. E. J. Heller, *Acc. Chem. Res.* **14**, 368 (1981).
50. A. R. Walton and D. E. Manolopoulos, *Chem. Phys. Lett.* **244**, 448 (1995).
51. S. M. Anderson, T. J. Park, and D. Neuhauser, *Phys. Chem. Chem. Phys.* **1**, 1343 (1998).
52. S. M. Anderson, J. I. Zink, and D. Neuhauser, *Chem. Phys. Lett.* **291**, 387 (1999).
53. A. E. Cardenas and R. D. Coalson, *Chem. Phys. Lett.* **265**, 71 (1997).
54. A. E. Cardenas, R. Krems, and R. D. Coalson, *J. Phys. Chem. A* **103**, 9569 (1999).
55. S.-I. Sawada, R. Heather, B. Jackson, and H. Metiu, *J. Chem. Phys.* **83**, 3009 (1985).
56. S. Sawada and H. Metiu, *J. Chem. Phys.* **84**, 227 (1986).
57. H.-D. Meyer and W. H. Miller, *J. Phys. Chem.* **70**, 3214 (1979).
58. H.-D. Meyer, *Chem. Phys.* **82**, 199–205 (1983).
59. G. D. Billing, *Int. Rev. Phys. Chem.* **13**, 309 (1994).
60. G. Stock, *J. Chem. Phys.* **103**, 1561–1573 (1995).
61. P. Kramer and M. Saraceno, *Lecture Notes in Physics*, Vol. 140, *Geometry of the Time-Dependent Variational Principle*, Springer, Berlin, 1981.
62. E. Deumens, A. Diz, R. Longo, and Y. Ohrn, *Rev. Mod. Phys.* **66**, 917 (1994).
63. E. J. Heller, *J. Chem. Phys.* **64**, 63 (1976).
64. R. T. Skodje and D. G. Truhlar, *J. Chem. Phys.* **80**, 3123 (1984).

65. R. C. Brown and E. J. Heller, *J. Chem. Phys.* **75**, 186 (1981).
66. M. Ben-Nun, T. J. Martínez, and R. D. Levine, *Chem. Phys. Lett.* **270**, 319–326 (1997).
67. M. Ben-Nun, T. J. Martínez, and R. D. Levine, *J. Phys. Chem.* **101A**, 7522 (1997).
68. G. C. Schatz and M. A. Ratner, *Quantum Mechanics in Chemistry*, Prentice-Hall, Englewood Cliffs, NJ, 1993.
69. R. K. Preston and J. C. Tully, *J. Chem. Phys.* **54**, 4297 (1971).
70. M. F. Herman and E. Kluk, *Chem. Phys.* **91**, 27 (1984).
71. J. Matthews and R. L. Walker, *Mathematical Methods of Physics*, W. A. Benjamin, New York, 1990.
72. K. Ruedenberg, *J. Chem. Phys.* **19**, 1433 (1951).
73. T. J. Martínez and R. D. Levine, *Chem. Phys. Lett.* **259**, 252 (1996).
74. T. J. Martínez and R. D. Levine, *J. Chem. Soc. Faraday Trans.* **93**, 940 (1997).
75. M. F. Trotter, *Proc. Am. Math. Soc.* **10**, 545 (1959).
76. E. C. G. Stueckelberg, *Helv. Phys. Acta.* **5**, 369 (1932).
77. E. E. Nikitin, *Theory of Elementary Atomic and Molecular Processes in Gases*, Clarendon, Oxford, 1974.
78. R. P. Feynman and A. R. Hibbs, *Quantum Mechanics and Path Integrals*, McGraw-Hill, New York, 1965.
79. R. P. Feynman, *Statistical Mechanics*, Addison-Wesley, Redwood City, CA, 1972.
80. L. S. Schulman, *Techniques and Applications of Path Integration*, Wiley, New York, 1981.
81. H. Kleinert, *Path Integrals in Quantum Mechanics*, World Scientific, Singapore, 1990.
82. B. J. Berne and D. Thirumalai, *Annu. Rev. Phys. Chem.* **37**, 401 (1986).
83. M. J. Gillan, in *Computer Modelling of Fluids, Polymers, and Solids*, C. R. A. Catlow, S. C. Parker, and M. P. Allen, eds., Kluwer, Dordrecht, 1990.
84. D. M. Ceperley, *Rev. Mod. Phys.* **67**, 279 (1995).
85. N. Makri, *Comp. Phys. Commun.* **63**, 389 (1991).
86. M. E. Tuckerman, B. J. Berne, G. J. Martyna, and M. L. Klein, *J. Chem. Phys.* **99**, 2796 (1993).
87. D. Chandler and P. G. Wolynes, *J. Chem. Phys.* **74**, 4078 (1981).
88. M. E. Tuckerman, D. Marx, M. L. Klein, and M. Parrinello, *J. Chem. Phys.* **104**, 5579 (1996).
89. D. Marx and M. Parrinello, *J. Chem. Phys.* **104**, 4077 (1996).
90. M. E. Tuckerman, D. Marx, M. L. Klein, and M. Parrinello, *J. Chem. Phys.* **104**, 5579–5588 (1996).
91. M. E. Tuckerman, D. Marx, M. L. Klein, and M. Parrinello, *Science* **275**, 817 (1997).
92. M. E. Tuckerman and G. J. Martyna, *J. Phys. Chem. B* **104**, 159–178 (2000).
93. M. Shiga, M. Tachikawa, and S. Miura, *Chem. Phys. Lett.* **332**, 396–402 (2000).
94. M. Pavese, D. R. Berard, and G. A. Voth, *Chem. Phys. Lett.* **300**, 93 (1999).
95. J. C. Tully and R. K. Preston, *J. Chem. Phys.* **55**, 562 (1971).
96. J. C. Tully, *J. Chem. Phys.* **93**, 1061 (1990).
97. N. Makri and W. H. Miller, *J. Chem. Phys.* **91**, 4026 (1989).
98. T. D. Sewell, Y. Guo, and D. L. Thompson, *J. Chem. Phys.* **103**, 8557 (1995).
99. T. Vreven, F. Bernardi, M. Garavelli, M. Olivucci, M. A. Robb, and H. B. Schlegel, *J. Am. Chem. Soc.* **119**, 12687–12688 (1997).

100. M. Hartmann, J. Pittner, and V. Bonacic-Koutecky, *J. Chem. Phys.* **114**, 2123–2136 (2001).
101. M. Ben-Nun and T. J. Martínez, *J. Phys. Chem.* **103**, 6055 (1999).
102. M. F. Herman, *Annu. Rev. Phys. Chem.* **45**, 83–111 (1994).
103. N. Corbin and K. Singer, *Mol. Phys.* **46**, 671 (1982).
104. D. Hsu and D. F. Coker, *J. Chem. Phys.* **96**, 4266 (1992).
105. F. Arickx, J. Broeckhove, E. Kesteloot, L. Lathouwers, and P. Van Leuven, *Chem. Phys. Lett.* **128**, 310 (1986).
106. K. Singer and W. Smith, *Mol. Phys.* **57**, 761 (1986).
107. R. Heather and H. Metiu, *Chem. Phys. Lett.* **118**, 558 (1985).
108. R. Heather and H. Metiu, *J. Chem. Phys.* **84**, 3250 (1986).
109. K. G. Kay, *J. Chem. Phys.* **101**, 2250 (1994).
110. D. J. Tannor and S. Garashchuk, *Annu. Rev. Phys. Chem.* **51**, 553–600 (2000).
111. M. F. Herman, *J. Chem. Phys.* **85**, 2069 (1986).
112. W. H. Miller, *J. Phys. Chem.* **105**, 2942–2955 (2001).
113. X. Sun and W. H. Miller, *J. Chem. Phys.* **106**, 6346 (1997).
114. B. Jackson and H. Metiu, *J. Chem. Phys.* **85**, 4129 (1986).
115. S.-I. Sawada and H. Metiu, *J. Chem. Phys.* **84**, 6293 (1986).
116. R. D. Coalson, *J. Phys. Chem.* **100**, 7896 (1996).
117. C. C. Martens and J. Y. Fang, *J. Chem. Phys.* **106**, 4918 (1997).
118. A. Donoso and C. C. Martens, *J. Phys. Chem.* **102**, 4291 (1998).
119. C.-C. Wan and J. Schofield, *J. Chem. Phys.* **112**, 4447 (2000).
120. R. Kapral and G. Ciccotti, *J. Chem. Phys.* **110**, 8919 (1999).
121. C.-C. Wan and J. Schofield, *J. Chem. Phys.* **113**, 7047 (2000).
122. M. Ben-Nun and T. J. Martínez, *J. Phys. Chem.* **103**, 10517 (1999).
123. O. V. Prezhdo and P. J. Rossky, *J. Chem. Phys.* **107**, 825 (1997).
124. M. D. Hack, A. M. Wensmann, D. G. Truhlar, M. Ben-Nun, and T. J. Martínez, *J. Chem. Phys.* **115**, 000 (2001).
125. K. Thompson and T. J. Martínez, *J. Chem. Phys.* **110**, 1376 (1998).
126. M. Ben-Nun and T. J. Martínez, *J. Chem. Phys.* **112**, 6113 (1999).
127. J. Ischtwan and M. A. Collins, *J. Chem. Phys.* **100**, 8080 (1994).
128. M. J. T. Jordan, K. C. Thompson, and M. A. Collins, *J. Chem. Phys.* **102**, 5647 (1995).
129. M. J. T. Jordan, K. C. Thompson, and M. A. Collins, *J. Chem. Phys.* **103**, 9669 (1995).
130. M. J. T. Jordan and M. A. Collins, *J. Chem. Phys.* **104**, 4600 (1996).
131. M. A. Collins, *Adv. Chem. Phys.* **93**, 389–453 (1996).
132. M. A. Collins and K. C. Thompson, in *Chemical Group Theory: Techniques and Applications*, Vol. 4, D. Bonchev and D. H. Rouvray, eds., Gordon and Breach, Reading, MA, 1995, p. 191.
133. K. C. Thompson and M. A. Collins, *J. Chem. Soc. Faraday Trans.* **93**, 871 (1997).
134. R. A. Marcus and M. E. Coltrin, *J. Chem. Phys.* **67**, 2609 (1977).
135. C. J. Cerjan, S. Shi, and W. H. Miller, *J. Phys. Chem.* **86**, 2244 (1982).
136. D. G. Truhlar, A. I. Isaacson, and B. C. Garrett, in *Theory of Chemical Reaction Dynamics*, Vol. 4, M. Baer, ed., CRC Press, Boca Raton, FL, 1985.
137. G. C. Lynch, D. G. Truhlar, and B. C. Garrett, *J. Chem. Phys.* **90**, 3102 (1989).

138. M. Ben-Nun and T. J. Martínez, *J. Phys. Chem.* **102A**, 9607 (1998).
139. M. Ben-Nun, F. Molnar, H. Lu, J. C. Phillips, T. J. Martínez, and K. Schulten, *Faraday Disc.* **110**, 447 (1998).
140. T. J. Martínez, *Chem. Phys. Lett.* **272**, 139 (1997).
141. C. F. Melius and W. A. Goddard, III, *Phys. Rev. A* **10**, 1528 (1974).
142. *Gaussian Basis Sets for Molecular Calculations*, Vol. 0, S. Huzinaga, ed., Elsevier, Amsterdam, 1984.
143. E. Teller, *Isr. J. Chem.* **7**, 227 (1969).
144. G. J. Atchity, S. S. Xantheas, and K. Ruedenberg, *J. Chem. Phys.* **95**, 1862 (1991).
145. U. Manthe and H. Koppel, *J. Chem. Phys.* **93**, 1658 (1990).
146. R. Baer, D. Charutz, R. Kosloff, and M. Baer, *J. Chem. Phys.* **105**, 9141 (1996).
147. D. R. Yarkony, *J. Chem. Phys.* **114**, 2601–2613 (2001).
148. G. Orlandi, F. Zerbetto, and M. Z. Zgierski, *Chem. Rev.* **91**, 867 (1991).
149. B. A. Balko, J. Zhang, and Y. T. Lee, *J. Phys. Chem.* **101**, 6611 (1997).
150. E. M. Evleth and A. Sevin, *J. Am. Chem. Phys.* **103**, 7414–7422 (1981).
151. J. R. McNesby and H. Okabe, *Adv. Photochem.* **3**, 228 (1964).
152. P. Farmanara, V. Stert, and W. Radloff, *Chem. Phys. Lett.* **288**, 518 (1998).
153. P. G. Wilkinson and R. S. Mulliken, *J. Chem. Phys.* **23**, 1895 (1955).
154. R. McDiarmid and E. Charney, *J. Chem. Phys.* **47**, 1517 (1967).
155. P. D. Foo and K. K. Innes, *J. Chem. Phys.* **60**, 4582 (1974).
156. R. J. Buenker and S. D. Peyerimhoff, *Chem. Phys.* **9**, 75–89 (1976).
157. A. J. Merer and R. S. Mulliken, *Chem. Rev.* **69**, 639 (1969).
158. R. S. Mulliken, *J. Chem. Phys* **66**, 2448–2451 (1977).
159. W. Siebrand, F. Zerbetto, and M. Z. Zgierski, *Chem. Phys. Lett.* **174**, 119 (1990).
160. J. Ryu and B. S. Hudson, *Chem. Phys. Lett.* **245**, 448 (1995).
161. V. Bonacic-Koutecky, P. Bruckmann, P. Hiberty, J. Koutecky, C. Leforestier, and L. Salem, *Angew. Chem. Int. Ed. Engl.* **14**, 575 (1975).
162. L. Salem and P. Bruckmann, *Nature* **258**, 526–528 (1975).
163. L. Salem, *Science* **191**, 822–830 (1976).
164. C. Longstaff, R. D. Calhoon, and R. R. Rando, *Proc. Natl. Acad. Sci. USA* **83**, 4209–4213 (1986).
165. B. R. Brooks and H. F. Schaefer III, *J. Am. Chem. Soc.* **101**, 307–311 (1979).
166. R. J. Buenker, V. Bonacic-Koutecky, and L. Pogliani, *J. Chem. Phys.* **73**, 1836–1849 (1980).
167. R. J. Sension and B. S. Hudson, *J. Chem. Phys.* **90**, 1377–1389 (1989).
168. A. H. H. Chang, A. M. Mebel, X. M. Yang, S. H. Lin, and Y. T. Lee, *Chem. Phys. Lett.* **287**, 301 (1998).
169. V. D. Knyazev and I. R. Slagle, *J. Phys. Chem.* **100**, 16899 (1996).
170. M. M. Gallo, T. P. Hamilton, and H. F. Schaefer III, *J. Am. Chem. Soc.* **112**, 8714–8719 (1990).
171. J. H. Jensen, K. Morokuma, and M. S. Gordon, *J. Chem. Phys.* **100**, 1981–1987 (1994).
172. E. F. Cromwell, A. Stolow, M. J. J. Vrakking, and Y. T. Lee, *J. Chem. Phys.* **97**, 4029 (1992).
173. B. A. Balko, J. Zhang, and Y. T. Lee, *J. Chem. Phys.* **97**, 935–942 (1992).
174. A. Stolow, B. A. Balko, E. F. Cromwell, J. Zhang, and Y. T. Lee, *J. Photochem. Photobiol.* **62**, 285 (1992).
175. S. Satyapal, G. W. Johnston, R. Bersohn, and I. Oref, *J. Chem. Phys.* **93**, 6398 (1990).

176. R. B. Woodward and R. Hoffmann, *Ang. Chem. Int. Ed. Eng.* **8**, 781 (1969).
177. W. A. Goddard III, *J. Am. Chem. Soc.* **92**, 7520–7521 (1970).
178. W. A. Goddard III, *J. Am. Chem. Soc.* **94**, 793–807 (1972).
179. H. E. Zimmerman, *Acc. Chem. Res.* **4**, 272 (1971).
180. J. E. Baldwin and S. M. Krueger, *J. Am. Chem. Soc.* **91**, 6444 (1969).
181. W. G. Dauben, J. Rabinowitz, N. D. Vietmeyer, and P. H. Wendschuh, *J. Am. Chem. Soc.* **94**, 4285 (1972).
182. C. W. Spangler and R. P. Hennis, *Chem. Commun.*, 24 (1972).
183. M. O. Trulson, G. D. Dollinger, and R. A. Mathies, *J. Am. Chem. Soc.* **109**, 586 (1987).
184. M. O. Trulson, G. D. Dollinger, and R. A. Mathies, *J. Chem. Phys.* **90**, 4274 (1989).
185. W. J. Leigh, *Can. J. Chem.* **71**, 147 (1993).
186. N. C. Craig, S. S. Borick, T. Tucker, and Y.-Z. Xia, *J. Phys. Chem.* **95**, 3549 (1991).
187. K. B. Wiberg and R. E. Rosenberg, *J. Phys. Chem.* **96**, 8282 (1992).
188. M. K. Lawless, S. D. Wickham, and R. A. Mathies, *J. Am. Chem. Soc.* **116**, 1593 (1994).
189. M. K. Lawless, S. D. Wickham, and R. A. Mathies, *Acc. Chem. Res.* **28**, 493 (1995).
190. R. C. Lord and D. G. Rea, *J. Am. Chem. Soc.* **79**, 2401 (1957).
191. F. Negri, G. Orlandi, F. Zerbetto, and M. Z. Zgierski, *J. Chem. Phys.* **103**, 5911 (1995).
192. W. Adam, T. Oppenlander, and G. Zang, *J. Am. Chem. Soc.* **107**, 3921 (1985).
193. H.-J. Werner, P. J. Knowles, J. Almlöf, R. D. Amos, A. Berning, D. L. Cooper, M. J. O. Deegan, A. J. Dobbyn, F. Eckert, S. T. Elbert, C. Hampel, R. Lindh, A. W. Lloyd, W. Meyer, A. Nicklass, K. Peterson, R. Pitzer, A. J. Stone, P. R. Taylor, M. E. Mura, P. Pulay, M. Schütz, H. Stoll, and T. Thorsteinsson (1998).
194. T. H. J. Dunning, *J. Chem. Phys.* **90**, 1007 (1989).
195. T. H. Dunning Jr. and P. J. Hay, in *Modern Theoretical Chemistry: Methods of Modern Electronic Structure Theory*, Vol. 3, H. F. Schaefer III, ed., Plenum, New York, 1977, p. 1.
196. R. A. Kendall, T. H. Dunning, Jr., and R. J. Harrison, *J. Chem. Phys.* **96**, 6796 (1992).
197. H. J. Werner and P. J. Knowles, *J. Chem. Phys.* **89**, 5803–5814 (1988).
198. P. J. Knowles and H. J. Werner, *Theor. Chim. Acta* **84**, 95–103 (1992).
199. I. Ohmine, *J. Chem. Phys.* **83**, 2348 (1985).
200. H. Koppel, W. Domcke, and L. S. Cederbaum, *Adv. Chem. Phys.* **57**, 59 (1984).
201. H. Koppel, L. S. Cederbaum, and W. Domcke, *J. Chem. Phys.* **89**, 2023 (1988).
202. A. Raab, G. A. Worth, H.-D. Meyer, and L. S. Cederbaum, *J. Chem. Phys.* **110**, 936 (1999).
203. H.-D. Meyer, U. Manthe, and L. S. Cederbaum, *Chem. Phys. Lett.* **165**, 73 (1990).
204. A. D. Hammerich, U. Manthe, R. Kosloff, H.-D. Meyer, and L. S. Cederbaum, *J. Chem. Phys.* **101**, 5623–5646 (1994).
205. U. Manthe, H.-D. Meyer, and L. S. Cederbaum, *J. Chem. Phys.* **97**, 3199–3213 (1992).
206. U. Manthe, *J. Chem. Phys.* **105**, 6989 (1996).
207. M. H. Beck, A. Jackle, G. A. Worth, and H.-D. Meyer, *Phys. Rep.* **324**, 1 (2000).
208. R. Schneider and W. Domeck, *Chem. Phys. Lett.* **150**, 235 (1988).
209. C. Woywod, W. Domcke, A. L. Sobolewski, and H.-J. Werner, *J. Chem. Phys.* **100**, 1400 (1994).
210. G. A. Worth, M. H. Beck, A. Jackle, and H.-D. Meyer, 2nd edition, University of Heidelberg, Heidelberg, 2000.
211. M. Ben-Nun and T. J. Martínez (work in progress).

212. D. E. Woon and T. H. Dunning, *J. Chem. Phys.* **98**, 1358 (1993).
213. A. Szabo and N. S. Ostlund, *Modern Quantum Chemistry*, McGraw-Hill, New York, 1989.
214. M. Ben-Nun, J. Quenneville, and T. J. Martínez, *J. Phys. Chem.* **104**, 5161 (2000).
215. J. Quenneville, M. Ben-Nun, and T. J. Martínez, *J. Photochem. Photobiol.* **144**, 229 (2001).
216. M. Ben-Nun and T. J. Martínez, *J. Am. Chem. Soc.* **122**, 6299 (2000).